FRICTION STIR WELDED MAGNESIUM

ALLOY AZ31B IN A LAP JOINT CONFIGURATION

By

Chase Davison Cox

Thesis

Submitted to the Faculty of the

Graduate School of Vanderbilt University

in partial fulfillment of the requirements

for the degree of

MASTER OF SCIENCE

in

Mechanical Engineering

August, 2010

Nashville, Tennessee

Approved:

Dr. Alvin Strauss   .

Dr. George Cook   .

Dr. David DeLapp   .

For my dogs Fiddler and Dottie.

ACKNOWLEDGEMENTS

TABLE OF CONTENTS

LIST OF FIGURES

LIST OF TABLES

LIST OF NOMENCLATURE

Symbol

FSW	Friction Stir Welding
HAZ	Heat Affected Zone
TMAZ	Thermomechanically Affected Zone
AZ31B	Mg Alloy
ρ	Density
T	Temperature
Z	Zener-Holloman Parameter
E	Strain
Q	Activation Energy
R	Universal Gas Constant
d	Grain diameter within TMAZ
TWI	The Welding Institute
RPM	Rotations Per Minute
IPM	Inches Per Minute
P	Power
Ω	Spindle Speed
Q	Heat input
B	Fraction of power dissipated by the tool
JLR	Joint Line Remnant
CFD	Computational Fluid Dynamics
A	Material Constant (1/s)
σ	Stress
σ_R	Effective stress
n	Material Constant (dimensionless)

CHAPTER I

INTRODUCTION

Friction Stir Welding (FSW) is a solid state joining process that utilizes the heat produced between the material and a non-consumable rotating pin to join the desired materials or work pieces. This rotation causes a plasticized region of material to rotate about the tool. As the tool is moved through the material, the material on the leading edge enters the plasticized region and is swept around to the back of the tool where the lagging material is left to form a solid joint. [Midling et. al, 1996] In order to obtain a properly consolidated weld it is also necessary for there to be a shoulder above the pin, typically 1.5-2 times the diameter of the pin, which rides along the surface of the work piece in intimate contact, while the pin is submerged in the work piece providing the stirring and heating. It is important to note that while the process is named Friction Stir Welding, friction is not the main source of energy for the weld but rather the shearing of the material at the interface between the tool and the material is.

FSW presents numerous advantages over conventional fusion welding techniques such as eliminating the need for a shielding gas, requiring less energy per weld, and the lack of a flame or arc making it safer in the work place. Another advantage of FSW is its ability to join materials that are extremely difficult, or impossible to weld with

conventional fusion techniques. Also, since FSW is a solid state process there is no melting of the parent material which can lead to the formation of unwanted and detrimental intermetallic compounds often present during the welding of dissimilar metals such as Magnesium and Aluminum. FSW is able to successfully join materials such as aerospace high alloy aluminums (2000 and 7000 series), magnesium, metal matrix composites, and dissimilar metals. Due to the advantages inherent to this process, FSW has been implemented by the automotive, aerospace, defense, and maritime industries. NASA has adopted FSW for use in the circumferential welds of the space shuttle's external fuel tanks. Other NASA applications of FSW include the Boeing Delta IV heavy rockets used to launch the Mars Phoenix Lander in July 2007. General Motors has begun funding research in FSW and has even started using FSW for some spot welding applications in production.

CHAPTER II

LITERATURE REVIEW

FSW Terminology
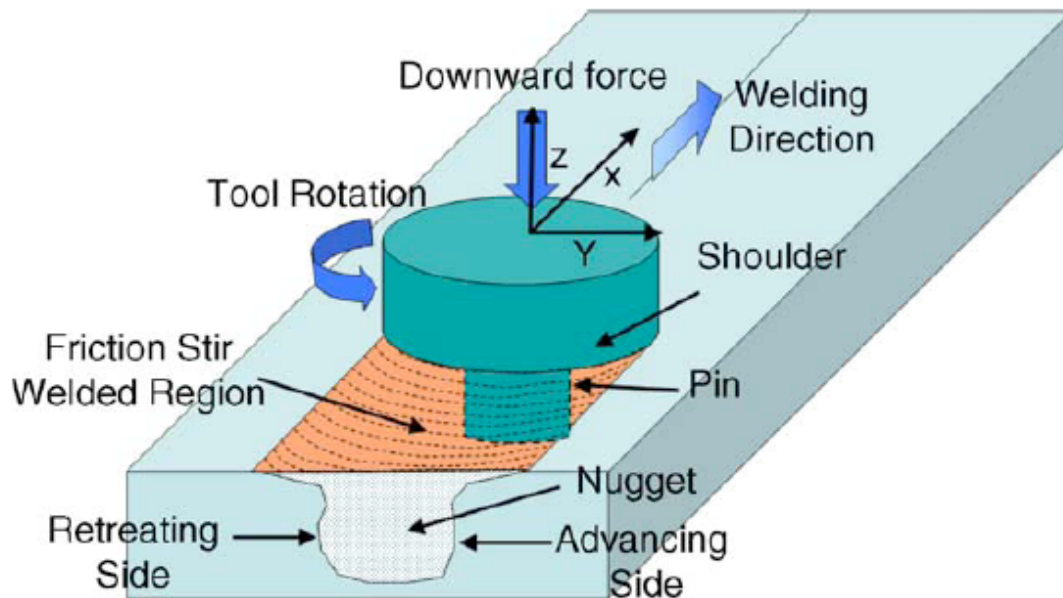
Figure 1 FSW diagram for typical butt weld configuration [Mishra 2005]

In FSW (See Figure 1) the tool can typically be described as having two parts and functions. The main part of the tool is the pin. The pin is the most important part of the tool in that it is submerged into the work piece (material to be welded.) It is the pin that

provides the stirring and heating of the work piece by both frictional heating and to a larger extent the shearing of the work piece. The shoulder is the other main part of the tool. The shoulder is placed in intimate contact with the work piece and also provides some frictional heating and contributes to the shearing of the work piece. It is the shoulder that provides the necessary pressure to successfully consolidate the welded material. The tool also has a larger shank that extends away from the work piece and allows for the Friction Stir Welding Machine to firmly grip and rotate the tool. The tool is typically placed at an angle with respect to the work piece (tilted $0° - 3°$ about the y-axis) such that the leading edge of the shoulder is slightly above the work piece, and the rear of the shoulder is slightly below the surface of the work piece. The part of the shoulder that is below the surface is known as the heel, and the amount of plunge experienced is called the heel plunge depth.

There are several terms used in FSW that help identify which part of the weld and tool are being discussed. When talking about the welding direction, this simply refers to the movement toward the unwelded material. More simply, it is the direction the pin appears to move relative to the backing anvil. The advancing and retreating sides of the weld can be defined by placing a tangential vector on the tool. The side of the tool in which the vector is in the same direction as that of the welding direction is called the advancing side, the side in which the vector is in the opposite direction is the retreating side. The nugget is the part of the weld that actually contains the sheared material. This is the zone that the tool affects mechanically and thermally.

In some instances there are tools with more intricate designs including those with fixed shoulders (to eliminate the heat input by the shoulder), threads and/or flutes on the

pin, non-axis symmetric pin design (Trivex) to increase stirring and shoulder features such as scrolls.

FSW Process Parameters

As in fusion welding, the feed rate is an important part of the process. When discussing the feed rate it is common to use the term "welding speed" or "traverse rate" to describe the translational speed of the tool. The term "Tool Rotation Speed" is used to classify the angular velocity (typically in rpm) of the tool. The direction of the tool is defined by looking down the tool towards the work piece, using the terminology "clockwise" and "counter (anti) clockwise." The Forces present in FSW are also an important parameter for the process. The force parallel with the axis of tool rotation (z component) is defined as the "down force." The force acting in parallel with the welding direction (x component) is known as the "traversing force", and the force perpendicular to this (y component) is known as the "side force" [Threadgill 2007.]

Weld Region Terminology

It is also common to discuss the weld area in FSW with specific terminology. In Figure 2, the region labeled as A is the parent material which is unaffected by the thermal and mechanical processes. The region labeled as B is known as the Heat Affected Zone (HAZ) and is only affected thermally. No stirring or shearing occurs in this zone. The next zone, C, is the Thermomechanically Affected Zone (TMAZ). The TMAZ extends from the advancing side HAZ to the retreating side HAZ. It is this zone that experiences

the mechanical shearing and thermal heating. For some metals such as aluminum the area

within the TMAZ may not be entirely recrystallized. In this case the recrystallized area is

contained within the zone labeled D is sometimes referred to as the as the "dynamically

recrystallized zone" but the term "Weld Nugget" is preferred. Recrystallization is a

process by which deformed grains are replaced by a new set of grains that nucleate and

grow until the original grains are entirely consumed. Recrystallization is dependent on a

critical temperature (different for each metal) and deformation. The recrystallization

temperature can be estimated by taking 0.4 times the melting point of the metal when

expressed on an absolute scale [DeGarmo 1997].
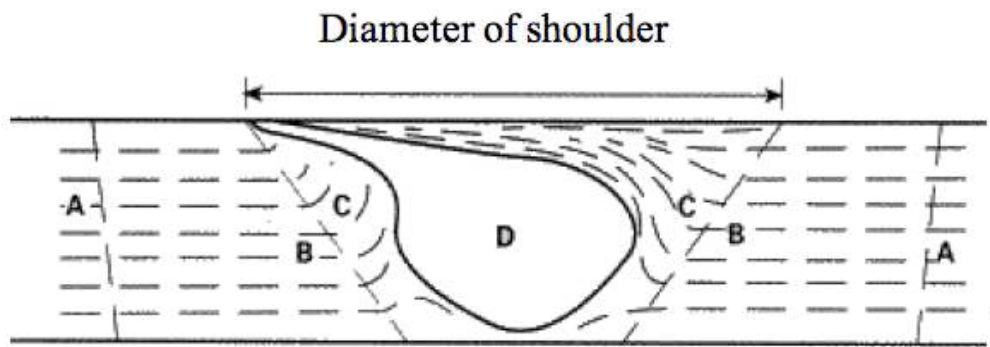
Figure 2 Graphical representation of weld zone [Nandan 2008]

For magnesium it can be difficult to distinguish the TMAZ and the nugget from

each other. The exact mechanism of recrystallization is not known but is not relevant to

microstructural classification [Threadgill 2007]. Figure 3.a represents a case when the

nugget is not easily distinguishable; 3.b shows the well formed nugget. The interface

between the weld zone and the base metal at the bottom of the weld is called the weld

root.
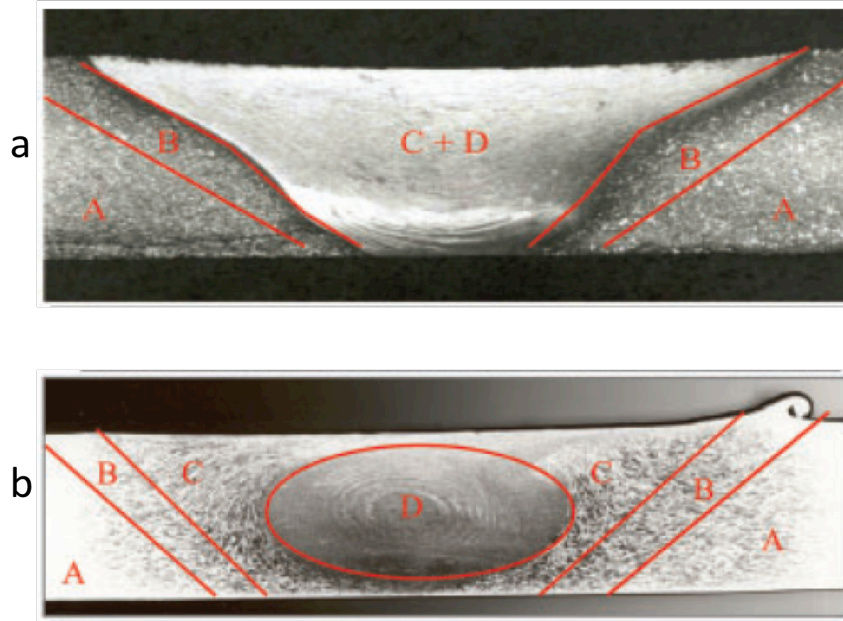
Figure 3 a: Cross section of Mg AM50 b: Cross section of Al 2014A-T6 indicating the 'zones' of FSW. b: shows the well formed nugget [Threadgill 2007]

Weld Joint Configuration
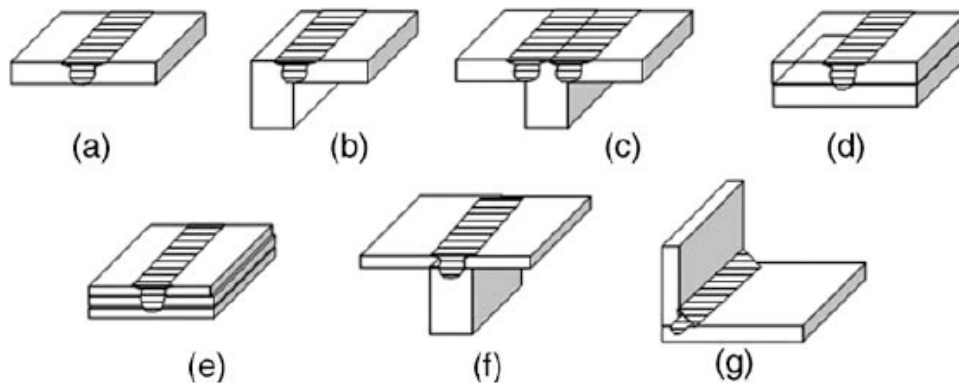
Figure 4 Standard weld configurations. a) square butt b) edge butt c) T joint butt d) lap joint e) multiple lap joint f) T lap joint g) fillet joint [Mishra 2005]
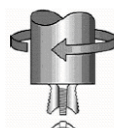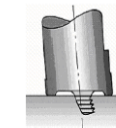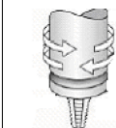
The most common weld configurations can be seen in Figure 4. For FSW, the

simple geometry of the butt joint (Fig 4.a) and lap joint (Fig 4.b) make them the most

commonly used configurations. For the butt joint the two separate work pieces of equal

thickness to be joined are placed on the backing anvil. To ensure that the pieces do not separate due to the large axial forces present during welding the two pieces are firmly clamped in place. The rotating tool is then plunged into the material until the shoulder has firm contact with the work piece, and is then traversed along the weld line. For the lap joint, the two work pieces to be joined are placed on top of one another (the pieces can be different thicknesses for this geometry.) The rotating tool is again plunged through the top plate (completely) so that some percentage of the length of the pin of the tool plunges into the bottom plate. The tool is then traversed through the material, resulting in the joining of the top plate to the bottom plate along the weld path. Other geometries not pictured would include pipe and spherical welding.

Tool Design and Implementation

One of the most important aspects of FSW is the design of the tool. The FSW tool affects the heat generation, material flow, power input, and weld quality. In the basic form, the shoulder provides the heating and restrains the material from leaving the weld zone, while both the pin and the shoulder contribute to the flow, or stirring of the material. The design of the tool can range from a smooth cylindrical pin with a flat shoulder to threads, flutes, flats, scrolls, etc., appearing on both the pin and shoulder. The pin can also have an asymmetrical shape. Tool design is driven by the application, such as reducing wear, reducing force, increasing stirring, increasing heating, etc. See table 1 for examples of more popular tool designs and their applications.

Table 1 Various tool designs from The Welding Institute [Nandan 2008]

Tool	Cylindrical	Whorl™	MX triflute™	Flared triflute™	A-skew™	Re-stir™
Schematics						
Tool pin shape	Cylindrical with threads	Tapered with threads	Threaded, tapered with three flutes	Tri-flute with flute ends flared out	Inclined cylindrical with threads	Tapered with threads
Ratio of pin volume to cylindrical pin volume	1	0.4	0.3	0.3	1	0.4
Swept volume to pin volume ratio	1.1	1.8	2.6	2.6	depends on pin angle	1.8
Rotary reversal	No	No	No	No	No	Yes
Application	Butt welding; fails in lap welding	Butt welding with lower welding torque	Butt welding with further lower welding torque	Lap welding with lower thinning of upper plate	Lap welding with lower thinning of upper plate	When minimum asymmetry in weld property is desired

Weld Quality

Manufacturing weld quality inspection distinguishes the differences between *imperfections*, *flaws* and *defects*. ASME standards define an *imperfection* in terms of a departure of a quality characteristic from its intended condition, and a *flaw* as an imperfection detectable by a non-destructive evaluation. A *defect* is defined as a flaw of prescribed shape, size, orientation, location or properties as to be rejected.

Volumetric flaws arise from a lack of material in friction stir welds. This defect is often referred to as porosity, but since the lack of material is not attributed to the formation of gas bubbles in the weld it is a misnomer, and the term void is preferred. The void can be described as being *buried, surface breaking, continuous* (such as a *wormhole*), *etc*. Voids are caused by insufficient material flow and can occur in various

sizes and locations. Another volumetric flaw is weld flash, occurring along the edges of the weld (most commonly the retreating side), which results in material being extruded at the top of the weld region rather than remaining within the weld. The appearance of excessive flash on a weld can be an indication of the formation of a void or worm hole.

Weld line flaws occur along the once planar interface between the two joined pieces. The appearance of sections of the joint line within the welded region is referred to as joint line remnant. The most serious type of this flaw occurs at the weld root. Flaws in the weld root can result from inadequate probe length, poor control of position/force, variations in work piece thickness, and local cooling. Weld imperfections, flaws, and defects can generally be eliminated (or at least significantly reduced) by insuring adequate flow, with proper process parameters for the material being welded, and tool geometry.

Material Properties and Characteristics: Mg AZ31B H24

Magnesium is an alkaline earth metal and is the sixth most abundant element in the Earth's crust (about 2% by mass) and the ninth most abundant in the Universe. By appearance, Mg is a silver/white metal and is typically coated with a thin oxide layer which reduces the metals reactivity giving it a dull and darkened appearance. The oxide layer also prevents corrosion, though Mg is readily corroded by chlorides and sulfates. Mg is also one the lightest naturally occurring metals (2/3 the density of aluminum) and has 94% of the tensile strength of aluminum.

The chemical composition of Mg AZ31B H24 can be seen in Table 2. The mechanical properties can be seen in Table 3.

Table 2 Chemical composition of Mg AZ31B

Material	%Al	% Cu	%Fe	%Mg	%Mn	%Ni	%Si	%Zn
AZ31B	2.5–3.5	0.05 max	0.005	balance	0.2 min	0.005 max	0.1 max	0.6 -1.4

Table 3 Material properties of Mg AZ31B

Material	Density	Tensile Strength	Yield Strength	Elastic Modulus	Poisson's Ratio
AZ31B	1.77 kg/m^	260 MPa	200 MPa	44.8 GPa	*0.35*

Mg is also a highly reactive metal, reacting with water at room temperature. Placing Mg in water at room temperature will result in the formation of hydrogen bubbles on the surface of the metal. Mg is also highly flammable when it is powdered or shaved into thin strips (such as flash resulting from a weld). Once ignited, Mg can continue to burn in an oxygen environment, a nitrogen environment, and in water. Mg is difficult to ignite in a bulk state. Special considerations for safety should be taken when working with and around Mg.

Mg AZ31B is said to have good machinability. Given the proper tooling geometry Mg can be cut quickly, machined to a good finish, and machined with less power than needed for aluminum or steel. The tool geometry plays an important role in chip formation and flow, heat generation, and material build up on the tool. Proper geometry can reduce the amount of wear on the tool and allow for higher feed rates. The tool should always be kept sharp when cutting/drilling because dull tools can result in excessive heat buildup, problems with dimensional tolerances, and sparking along the

tools edge. The power required to machine magnesium is 56% less than the power required to machine aluminum. This alloy is also suitable for welding using conventional welding techniques (gas shielded arc) [Elektron 2006].

The melting point of Mg is 650°C. The Mg alloy used for this research (AZ31B H24) has a slightly lower melting point of 630°C. As the temperature of the metal rises the material undergoes a linear decrease in density. Using the experiments of McGonigal et al. this linear change in the solid state ($\rho(T) = -2.05e^{-4}T + 1.77$) has been calculated and reported in table 4. The expression and values were approximated from Figure 5 [McGonigal 1961].

Table 4 Temperature dependent density of Mg

T (°C)	Density g/cm3
25	1.76
50	1.76
100	1.75
150	1.74
200	1.73
250	1.72
300	1.71
350	1.70
400	1.69
450	1.68
500	1.67
550	1.66
600	1.65
650	1.64
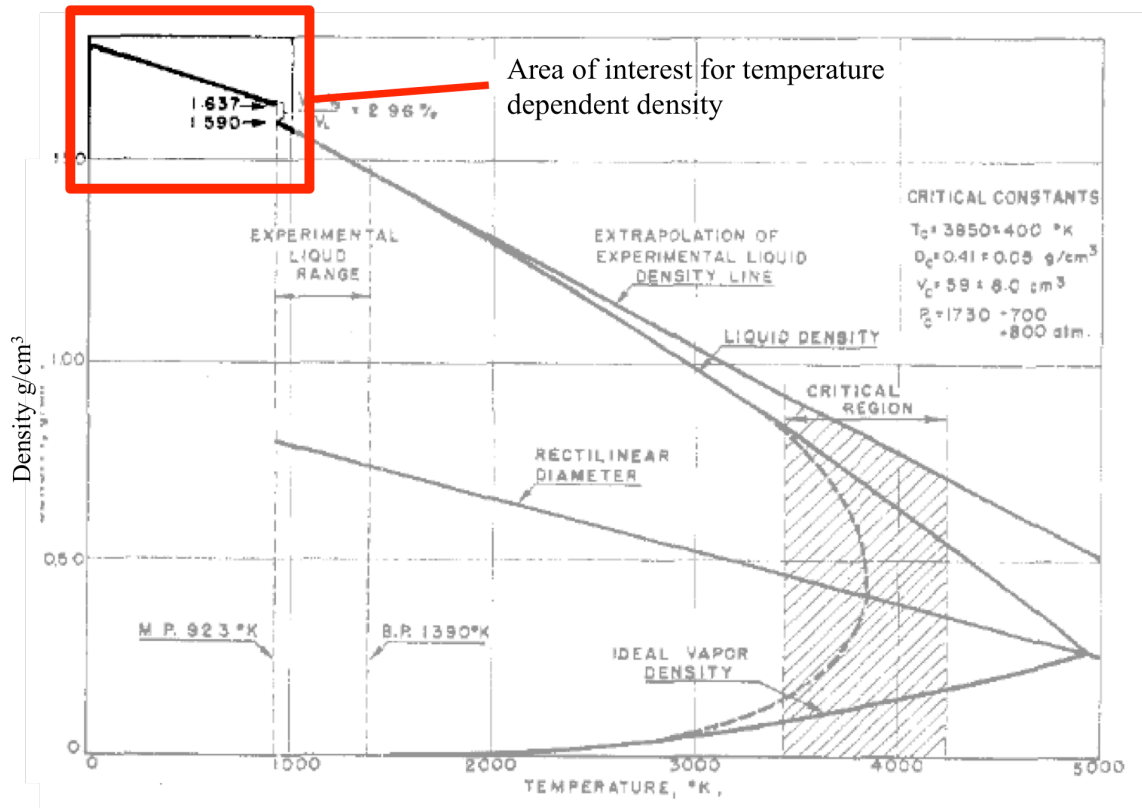
Figure 5 Liquid range diagram for Mg. Mg is reported as a solid to the threshold of 923°K (650°C) [McGonigal 1961]

Applications: Mg AZ31B H24

AZ31B in a sheet or plate has good applications in medium strength situations at temperatures at or below 300° F. Since the alloy is non-magnetic, it also finds application in the electronic industry as RFI and EMI shielding. Mg is also the third most commonly used structural metal (following steel and aluminum). High grade car wheels made from Mg alloy are called "MAG Wheels" which are significantly lighter than their steel or aluminum counterparts. Chevrolet and Mercedes-Benz made race cars in the 1950's with Mg alloy body panels which resulted in very light (and faster) automobiles. Porsche made the frame of their 917/053 automobile with a Mg alloy which won the 1971 Le Mans and

still holds the absolute distance record for this event. Volkswagen and Porsche both used Mg to make engine components including the engine block. More recently BMW used Mg in the engine blocks for their 1, 3, 5, 6, 7, Z4, Z5, X3 series automobiles in 2006 selling 300,000 units [Int. Mg 2007]. The 2006 Z06 Corvette engine cradle was made using Mg and in the process advanced the technology for manufacturing automotive parts from Mg [Magnesium 2010].

Microstructure of Mg AZ31B subjected to FSW process
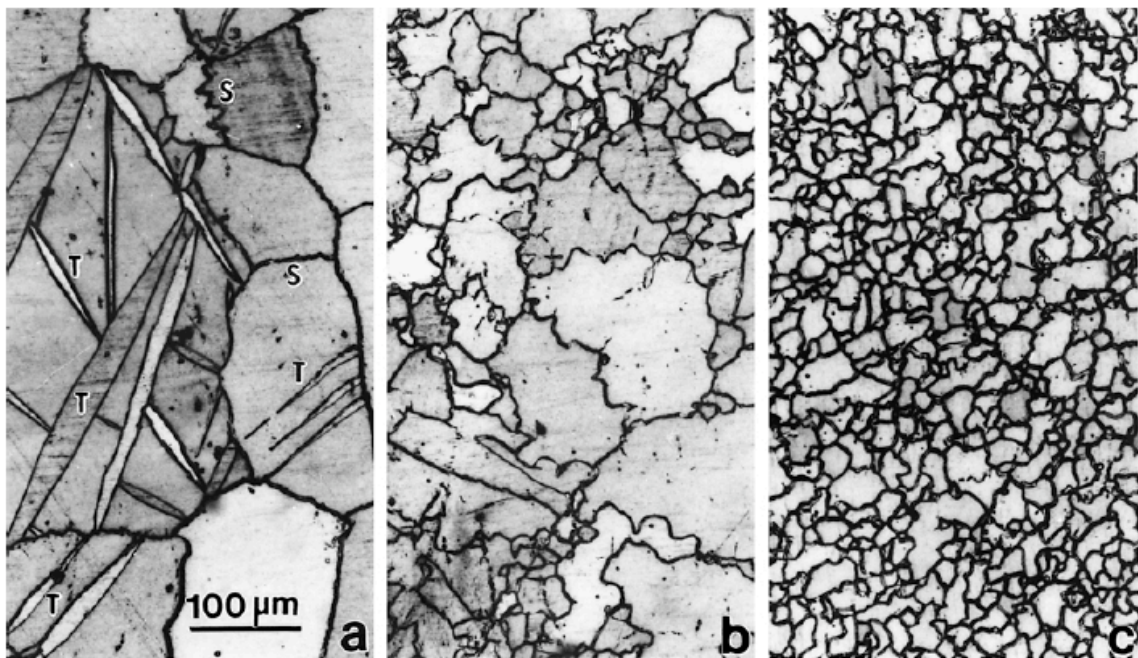
Figure 6 Comparison of microstructure in an FSW cross section. a) base metal b) transition zone c) weld zone (nugget) [Esparza 2002]

Figure 6 illustrates the evolution of grain size in MG AZ31B that has undergone the FSW process. The lighter areas of Figure 6 represent the grain (crystal) which

consists of a space occupied by a continuous crystal lattice. The dark lines surrounding

the grains are the grain boundaries. The term grain structure refers to the arrangement of

the grains of a specific crystal structure within the metal. The grain boundary is a region

of misalignment between the characteristic lattice of the grains which acts as an area of

separation. This area is usually one to three atoms in diameter (see Figure 7).
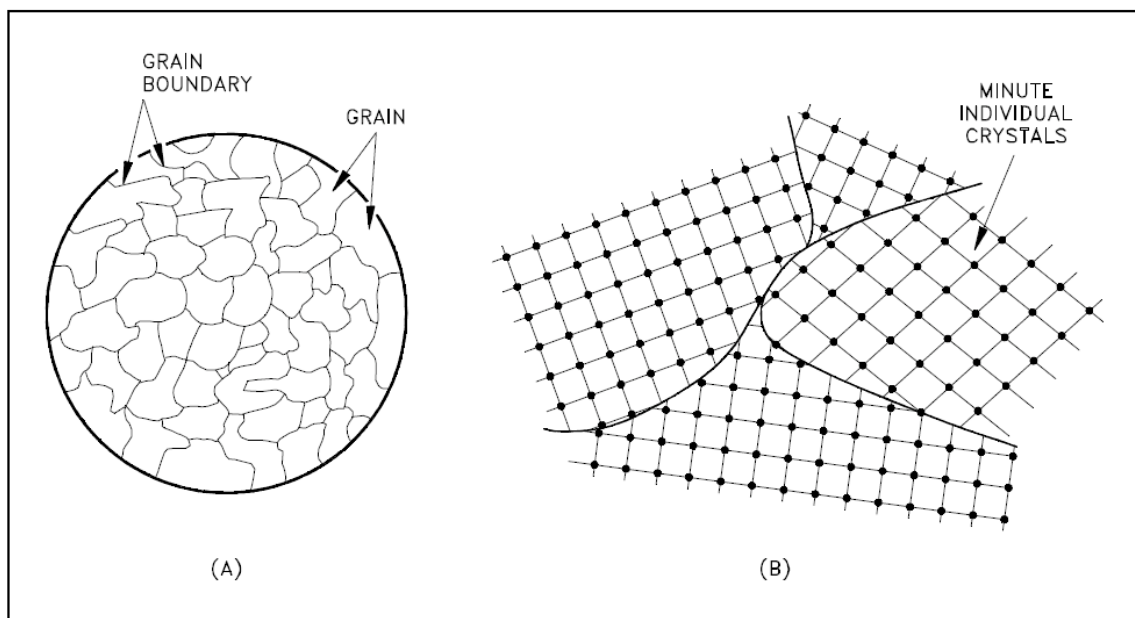
Figure 7 Grains and Boundaries a) microscopic b) atomic [DOE 1993]

The average size of the grain is an important feature for determining the mechanical

properties of the metal. A smaller grain size (more refined) increases the tensile strength

and ductility. A larger grain size increases creep; the permanent deformation that

increases with time under a constant load [DOE 1993.]

From Figure 6 it can be seen that the average grain size decreases significantly from the base metal (6a) to the transition zone (6b) and finally the weld zone (6c). It is also noted that numerous observations of deformation twins and serrations of the grain boundaries were made in the base metal. However these were eliminated within the weld zone where the recrystallized and equiaxed (uniform in size and dimension) grain structures occurred. Esparza et al. reported an average grain size of 175µm in the base material and an average grain size of 25µm in the weld zone [Esparza 2002].

Another experiment looked at the grain structure evolution during FSW and was performed by Pareek et al [Pareek 2007]. The experiment involved butt welding 3.175 mm plates of Mg AZ31B to itself at an array of welding speeds (3, 5, and 8 ipm) and rotation speeds (1500 and 2000 RPM). Microstructural evaluation of the surface of the base material and welded material produced the observation of dispersoids (particles of one material dispersed into another material) in the metal.
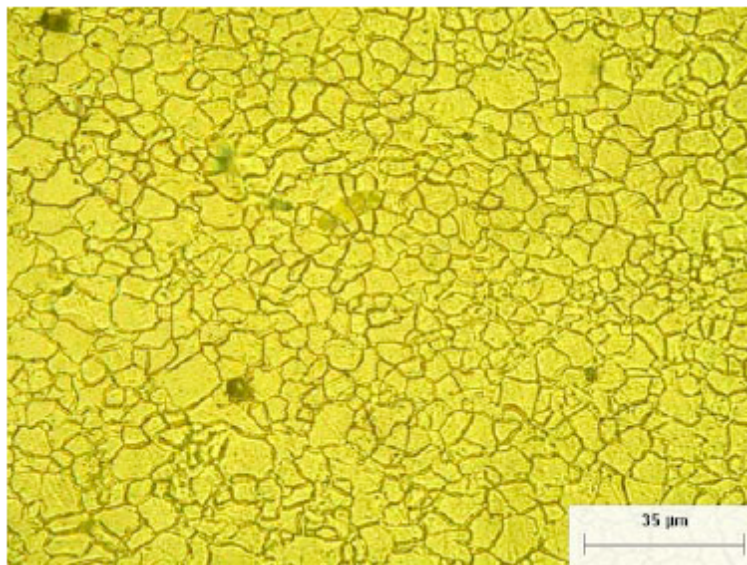
Figure 8 Photomicrograph of the as-received Mg Alloy [Pareek 2007]
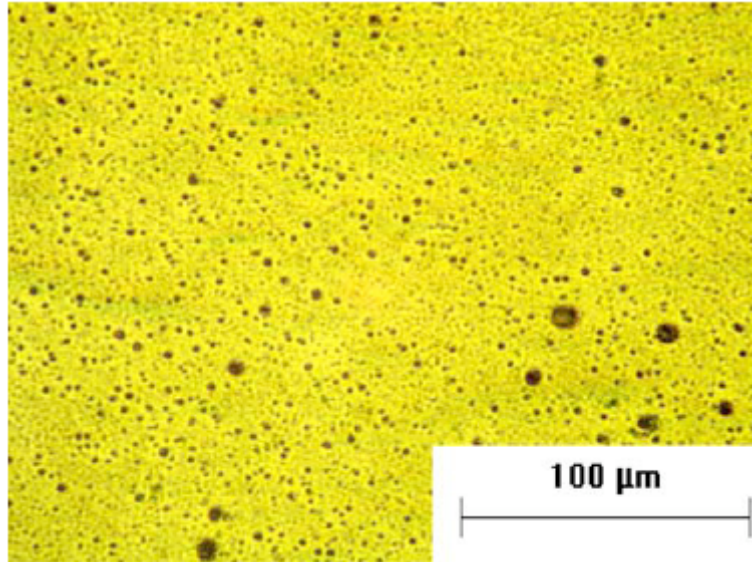
Figure 9 Dispersoids in the advancing side of weld [Pareek 2007]
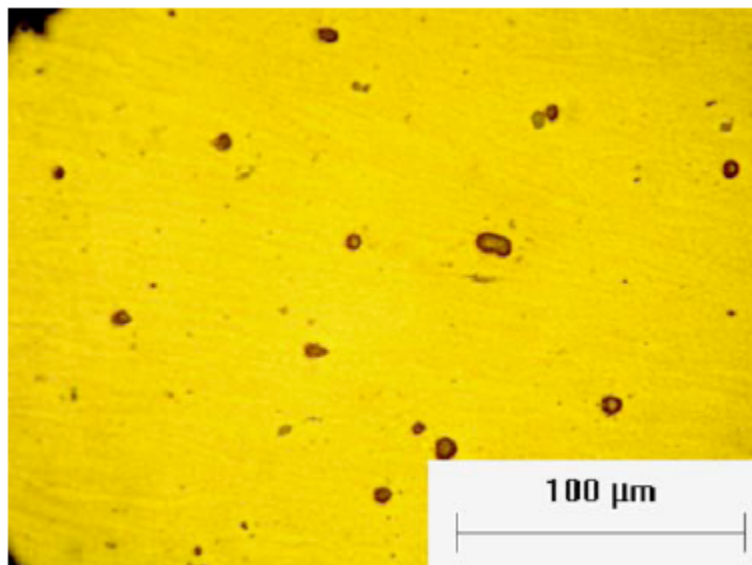
Figure 10 Dispersoids on the retreating side of the weld [Pareek 2007]

Pareek found that the smaller dispersoids were composed of 97.7 wt. % Mg and 2.3 wt. % O, or simply magnesium oxide. The larger particles contained Mn and Al in addition to Mg and O (68.3 wt. % Mg, 20.5 wt. % Mn, 9.0 wt. % Al, and 2.2 wt. % O). The increased occurrence of these dispersoids on the advancing side was found to be a result of the geometry of the flow of material resulting from the rotation of the tool.

Table 5 Volume fraction of dispersoids [Pareek 2007]

Parameter	% Volume Fraction	
	Advancing side	Retreating side
1500 rpm—1.3 mm/s (3 ipm)	1.91	0.60
1500 rpm—2.1 mm/s (5 ipm)	1.68	0.51
1500 rpm—3.4 mm/s (8 ipm)	2.57	1.03
2000 rpm—1.3 mm/s (3 ipm)	1.55	0.56
2000 rpm—2.1 mm/s (5 ipm)	2.51	0.59
2000 rpm—3.4 mm/s (8 ipm)	2.53	1.04

Table 5 shows the percentage of volume taken by the dispersoids by location as functions of the welding parameters. Although each of the welds in this study subjected to tensile evaluations broke on the advancing side no dispersoids were found on the fracture surfaces. This result suggests that the higher occurrence of the dispersoids on the advancing side did not affect the tensile strength but rather resulted from the heterogeneous microstructure at this location.

The effect of welding parameters on grain size showed that higher traverse rates resulted in a finer grain size and that higher rotation speeds resulted in a larger grain size.
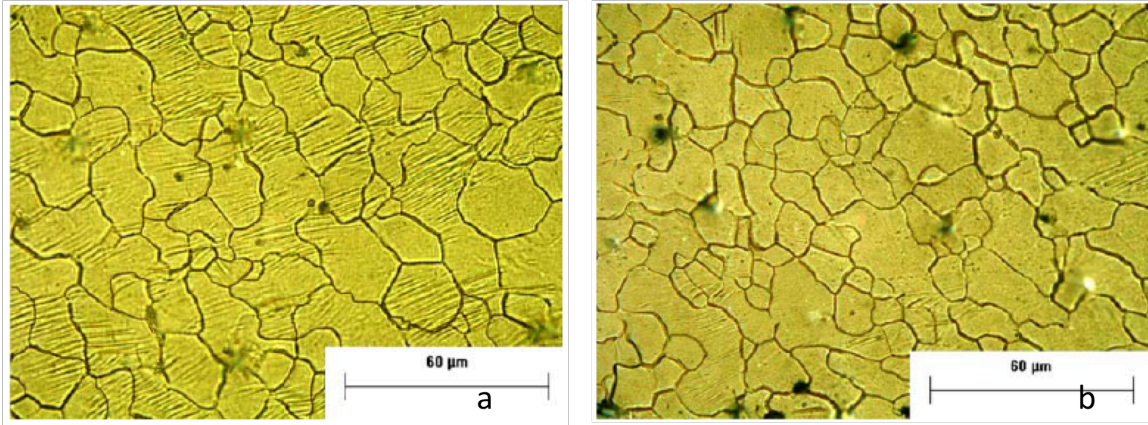
Figure 11 Grain microstructure from center of weld a) FSW at 1500 rpm and 3 ipm b) FSW at 2000 rpm and 8 ipm [Pareek 2007]

The decrease in the average grain diameter with increased welding (traverse) speeds was attributed to greater straining of the material which increased nucleation sites. The greater straining (deformation) of the metal (associated with the process parameters) imparts more energy into the metal which increases the creation of nucleation sites. As the nucleation rate (crystal formation) increases, the grain growth becomes more competitive, resulting in a finer average grain size. The increase in grain size with rotation speed was attributed to the higher temperatures associated with these higher rotation speeds [Pareek 2007].

The critical temperature for dynamic re-crystallization is related to temperature, strain, and strain rate. The Zener-Holloman parameter (Z) relates these variables as:

$$Z = \dot{\varepsilon} * \exp(\frac{Q}{RT})$$

Where $\dot{\varepsilon}$ is the strain rate of the area of interest (weld zone), Q is the activation energy (energy threshold) of Mg AZ31B (129 kJ/mol), R is the gas constant, and T is the absolute temperature. The activation energy physically represents the energy needed for

19

deformation and is closely related to the activation energy of self-diffusion and the

activation energy of creep [Spigarelli 2001]. Chang et al. established a relationship

between grain size and Z for friction stir processed Mg AZ31B:

$$\ln (d) = 9.0 - 0.27 \times \ln (Z)$$

Where d is the dynamically recrystallized grain size within the affected zone. This

empirical function shows that the average grain size would be refined with decreasing

weld zone temperatures and increasing strain rates. Figure 12 shows the grain refinement

of the weld and TMAZ zones for the array of welding parameters. The grain size, as

predicted, became more refined with increasing the traverse rate and with a decrease in

rotation speed. The grain refinement was less pronounced in the TMAZ [Pareek 2007].
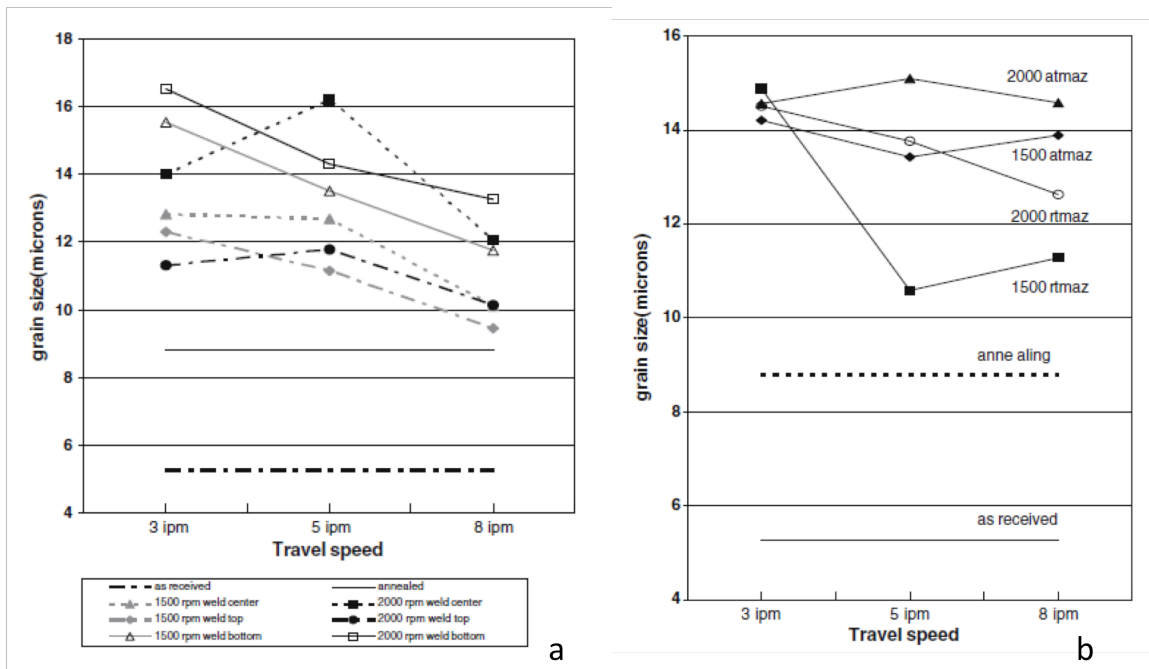
Figure 12 Grain size measurements a) inside the weld zone b) the advancing (atmaz) and retreating (rtmaz) TMAZ zones [Pareek 2007]

Tensile Properties of Mg AZ31B FSW Welds in Literature
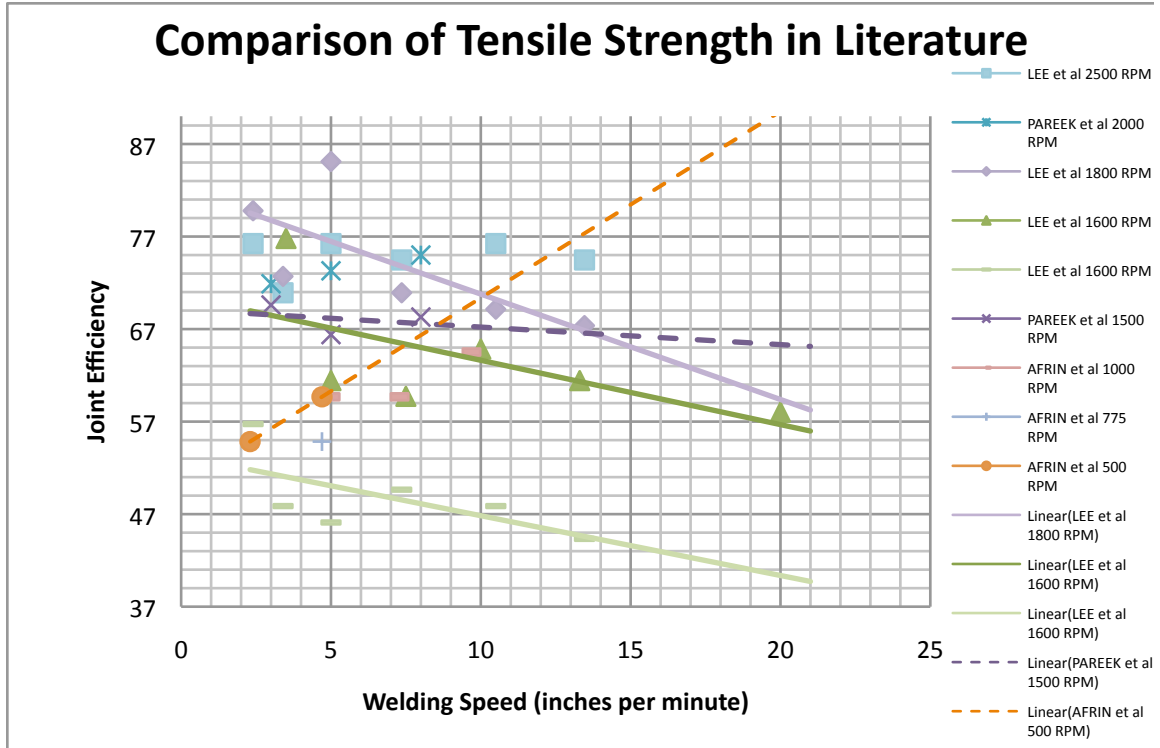
Figure 13 Reported tensile strength of Mg AZ31B FSW samples. Rotation speed is indicated in the key. Welding Speed is the x-axis. Joint Efficiency (% parent tensile strength) is the y-axis.

Figure 13 shows a general synopsis of a sampling of the data currently available for Mg AZ31B FSW experiments. The lines shown on the graph represent a linear best fit to the data in order to capture the general trend of each report. Lee et al. reported that tensile strength increased with rotation speed and decreased with welding speed [Lee 2003 & 2002]. However, Afrin et al. reported that yield and tensile strength increased with welding speed and decreased with rotation speed due to a reduction in the heat generated within the weld zone [Afrin 2008]. Cao et al. (the only study found performing lap joints) also reported that tensile strength increased with welding speed but added that a maximum welding speed of 15 mm/s but remained constant at faster speeds [Cao 2009]. The maximum reported tensile strength reported by Cao et al. was 52% of the

parent material. Comparisons will be made between the results in the literature and those of this research.

Experimental Equipment and Procedure: FSW Machine

The Friction Stir Welding machine used for this study is a converted 1940's era Kearney and Trecker Model K Number 2 three axis milling machine. The machine was retrofitted with three additional motors and a control system. The system controls the spindle speed and the traverse, lateral, and vertical movements of the table. The machine can be seen in Figure 14. The welding machine is controlled via a National Instruments data acquisition device and in house written software. Forces and Torques were measured via a Kistler cutting force dynamometer mounted rigidly between the spindle head and the tool holder.

When welding, the material is firmly clamped to the anvil in the appropriate geometry (lap, butt, etc.). The tool is then moved into position over the starting point of the weld. The spindle motor is then engaged to the appropriate RPM for the experiment and the table is raised (rotating tool is lowered) into the material at approximately 0.1 IPM. Once the tool is at the desired plunge depth the tool then traverses along the weld line. At the end of the weld the material is lowered (rotating tool is raised) and the weld is completed. The result of this leaves a "key hole" at the end of the weld which can be seen in Figure 15.

Figure 14 FSW Machine. CL: Clamps, TH: Tool Holder, ANV: Anvil, TM: Traverse Motor, VM: Vertical Motor, SM: Spindle Motor
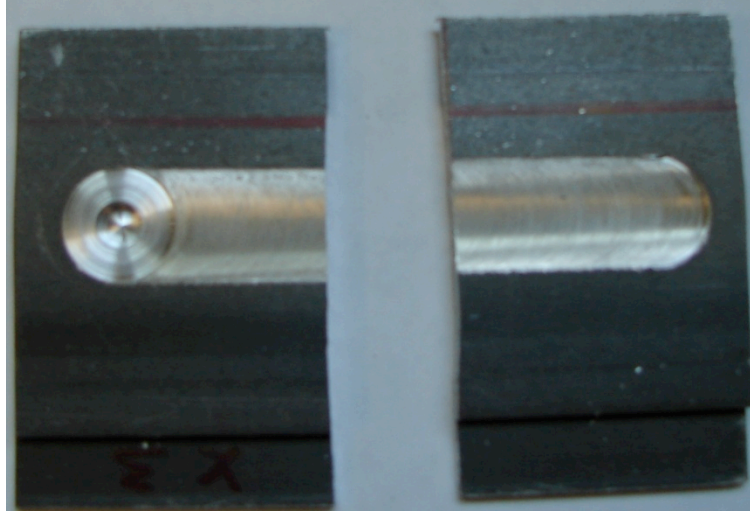
Figure 15 The left side of the image presents the resulting "Key Hole" effect when the tool is removed from the material. The right side of the image presents the result from plunging the tool into the material.

For safety purposes a large 5 gallon container of dry sand was kept on hand in the event that the magnesium was ignited. Mg readily reacts with water and would only intensify the fire if used as a suppressant. The sand would eliminate the oxygen supply of the ignited Mg.

CHAPTER III

EFFECTS OF ROTATION AND TRAVERSE SPEEDS ON LAP JOINTS OF FRICTION STIR WELDED Mg AZ31B H24

Introduction

Previous investigations of welding Mg AZ31B using FSW such as Lee et al. state that high rotation speeds (1600-2500 rpm) and low traverse speeds (0.2 – 6.0 inches per minute) are best for producing sound welds with a relatively high tensile strength (85% of parent material.) The weld joint configuration used in the Lee study was the butt joint. The butt joint requires that two materials of identical thickness be abutted to one another. The rotating tool then moves along the joint line. In a study by Cao et al. 0.078 in sheets of Mg AZ31B were joined using FSW in the lap joint configuration with full penetration. In this study it was shown that the welding speed had a large impact on the formation of hooking defects with lower speeds resulting in larger defects. The study also showed that the tensile strength of the welds was strongly correlated to the welding speed up to a traverse speed of 35 inches per minute [Cao 2009].

The goal for this investigation will be to produce reliable welds quickly such as those required in the automotive or aerospace industries, requiring higher welding and rotation speeds to meet the needs of high productivity and throughput. The effects of

welding speeds from 2 to 21 inches per minute on the quality of a lap joint will be evaluated based on tensile strength, hammer bend test, numerical modeling, and macro-section evaluation.

Experimental

The magnesium alloy of interest is a heat treated Mg - AZ31B H24, a wrought alloy, which has a substantial application in industry and has recently been qualified as a potential material for ballistic applications [Jones 2007].

For this experiment the lap weld joint configuration was used. Each welding sample consisted of 2 pieces of 9 in x 1 ½ in x 0.09 in AZ31B plate with a 1.5 in overlap. The plates were rigidly clamped to a steel anvil. See Figure 16 for the geometry of the weld. For each weld the FSW tool was rotated in a clockwise direction with the retreating side of the weld being closer to the lapped edge of the top plate (located at the left of the tool in Figure 16) also known as a left-handed lap weld.
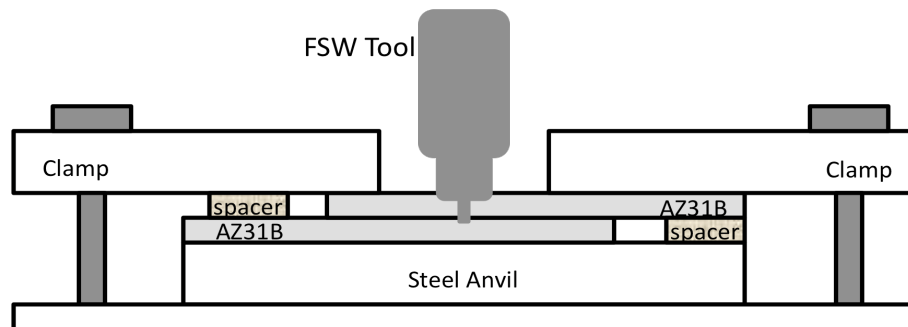
Figure 16: Experimental lap joint weld configuration

The FSW tool for this experiment was a modified Flared-triflute design[TM] based on the original design by The Welding Institute (TWI). The tool has a shoulder diameter of 0.625 in, a pin diameter of 0.250 in, and a pin length of 0.116 in. The length of the pin

allows for a complete penetration of the top plate with approximately 20% penetration into the bottom plate. A graphical representation of the tool used can be seen in Figure 17. The tool has a cupped feature in the center of the threaded flute geometry to better promote the desired material flow.
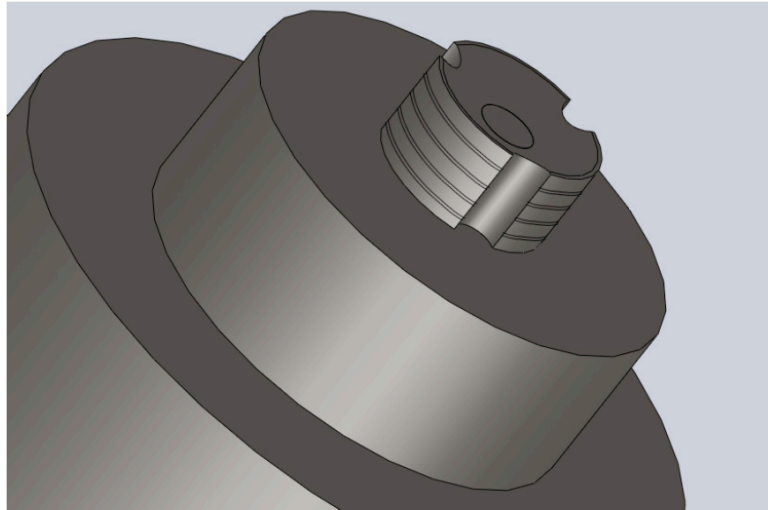
Figure 17: Graphic of the FSW tool. The modified Flared-triflute design™ has been used with the addition of a cup to the end of the pin [Hendricks 2009].

The material was prepped by removing the as-received wax like coating from both the top and bottom of each plate. This coating is put in place by the manufacture to help curb the reactivity of the metal to reduce the chances of it catching fire. Experiments were run in the Vanderbilt University Welding Automation Laboratory (VUWAL) facility to see if the inclusion of this coating in the process would affect the quality of the weld. Three samples were run for this experiment. The first was welded as received, the second was cleaned with alcohol, and the third was scrubbed to completely remove the coating. Each sample weld was performed at 2000 RPM and 6 IPM. The results of the tensile tests showed that there were no observable mechanical effects related to the

inclusion or exclusion of the coating. For the majority of the welds the coating was removed. Figures 18 and 19 illustrate the appearance of the metal as-received and cleaned of the coating.

Figure 18 Sample of as-received Mg AZ31B. Sample is 3"x9"x0.09" The coating on the material prevents the Mg alloy from reacting with the environment.
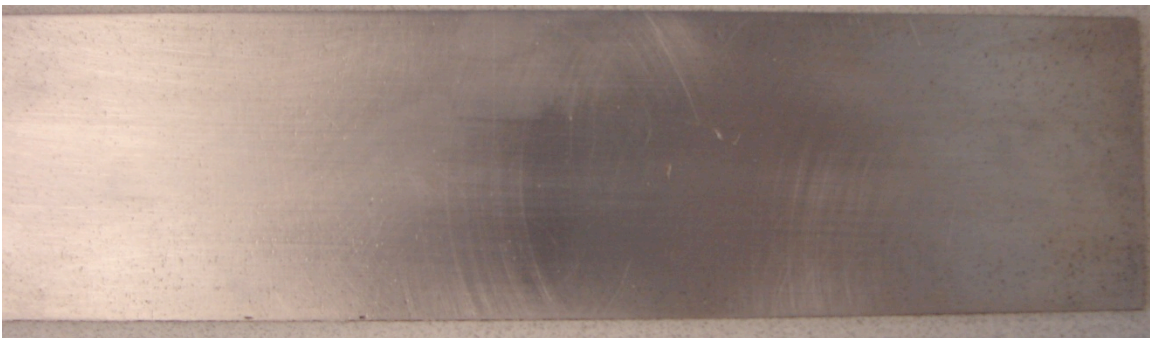
Figure 19 Sample of the cleaned Mg AZ31B. Sample is 3"x9"x0.09"

The lap joints were welded at both 1500 and 2000 RPM, a tilt angle of 1° for all welds, and a traverse rate of 2, 6, 10, 14, 18, and 21 inches per minute. The penetration depth was maintained such that the shoulder of the tool was held constant at 0.003 in below the surface of the top plate. The weld process involves lowering the rotating tool

into the material at 0.10 inches per minute until the proper plunge depth is achieved. The tool then remains at that location for 5 sec, followed by the tool traversing through the material.

1.5 inches were removed from the weld at the beginning and end to eliminate any transient welding conditions. Three 0.5 inch rectangular tensile shear specimens were taken from the beginning, middle, and end of each weld. A 0.75 inch wide section was taken from the beginning of the weld for the hammer bend test (see Figure 20.) The hammer bend test, as described by TWI, is a mechanical test specific to the lap weld configuration [TWI 2010]. The sample can either pass or fail the destructive test, which involved carefully hammering the sample such the top and bottom plates are subjected to a bending moment that puts a significant stress on the weld joint (see Appendix). A diagram of this test can be seen in Figure 26.
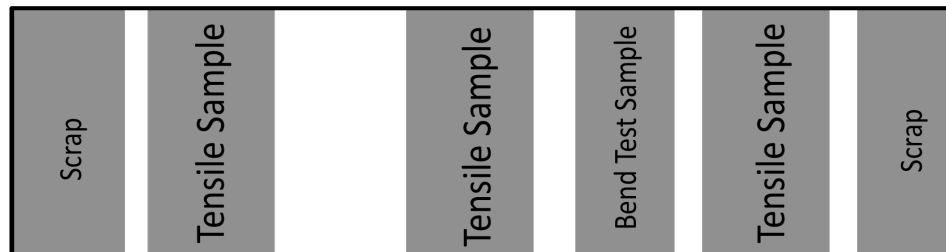
Figure 20: Layout of the different specimens obtained from each weld

Results and Discussion

Tensile Strength of Mg AZ31B Lap Welds

During the tensile tests for a lap joint the sample experiences a rotation that occurs during the evaluation due to the geometry of the specimen (see Figure 1 of the

Appendix). In order to compare the tensile strength of the results of this experiment to tensile strengths reported in the literature a base specimen was created to the same geometry as the weld tensile sample by machining a larger piece of AZ31B to the appropriate dimensions (see Figure 21). Three of these samples were made and the ultimate tensile strength of this geometry was experimentally determined to be 102.1 MPa. Each of the weld's three tensile samples were then tested for tensile strength and compared as a percentage to the base specimen's tensile strength.

Figure 21: AZ31B machined to match the dimension of the tensile specimens for a baseline comparison.
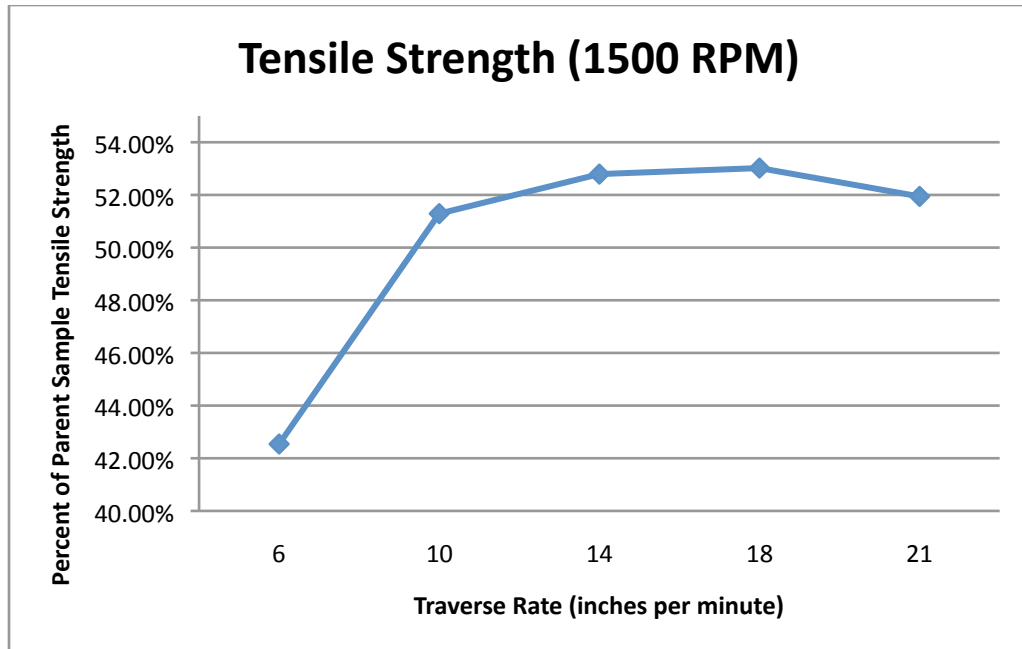
Figure 22: Resulting averaged ultimate tensile strength for welds at 1500 RPMs
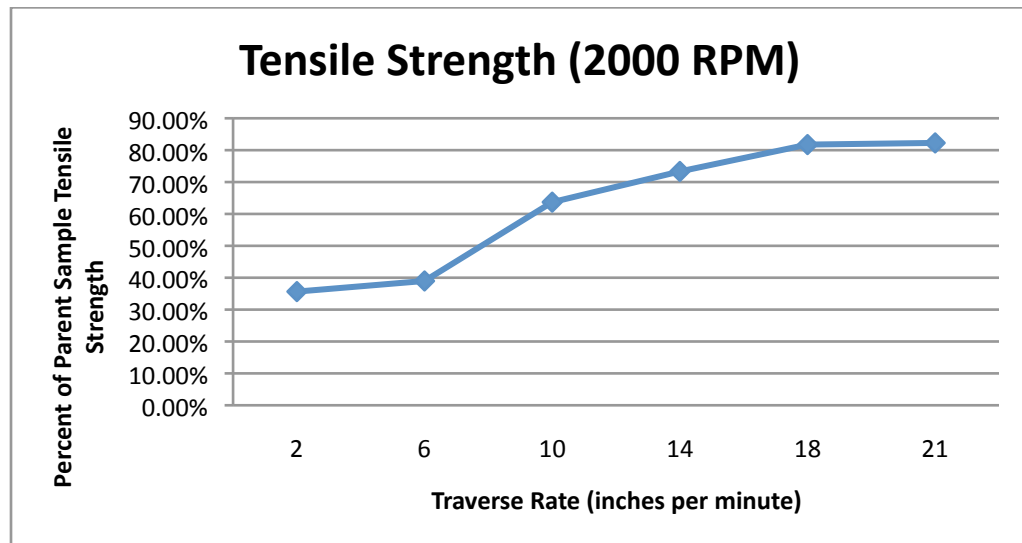
Figure 23: Resulting averaged ultimate tensile strength for welds at 2000 RPMs

Figures 22 and 23 show the results of the tensile tests for each of the welds. For the 1500 RPM welds it was found that the highest averaged ultimate tensile strength was only 53% of the parent sample and occurred at a traverse rate of 18 inches per minute.

For the 2000 RPM welds it was found that the highest averaged ultimate tensile strength was 82% of the parent sample and occurred at a traverse rate of 21 inches per minute. Table 6 shows the ultimate tensile strength of each weld sample. The samples A, B, and C represent a tensile coupon taken from the beginning, middle, and end respectively. The UTS is reported as a percentage of the parent sample and the standard deviation is reported in MPa.

Table 6 Ultimate Tensile Strength for each of the weld samples

Weld ID	IPM	RPM	UTS A	UTS B	UTS C	Avg. UTS	Std. Dev
Weld 6	2	2000	40.06%	33.59%	33.30%	35.65%	3.90
Weld 5	6	2000	35.55%	39.57%	41.82%	38.98%	3.24
Weld 1	10	2000	65.43%	62.78%	62.88%	63.70%	1.53
Weld 2	14	2000	85.60%	69.83%	64.54%	73.33%	11.18
Weld 7	18	2000	81.68%	76.89%	86.68%	81.75%	5.00
Weld 8	21	2000	81.39%	79.73%	85.70%	82.27%	3.15
Weld 9	6	1500	36.43%	43.78%	47.40%	42.54%	5.71
Weld 3	10	1500	44.96%	54.85%	54.06%	51.29%	5.61
Weld 4	14	1500	51.32%	53.97%	53.09%	52.79%	1.37
Weld 10	18	1500	50.54%	53.18%	55.34%	53.02%	2.45
Weld 11	21	1500	52.60%	50.93%	52.30%	51.94%	0.91

The maximum ultimate tensile strength for both the 1500 and 2000 RPM welds occurred at 18 inches per minute from the "C" tensile coupon and were 55.34% and 86.68% respectively. The lowest ultimate tensile strength for the 2000 RPM welds occurred at 2 inches per minute and was 33.3% of the parent sample. Note that no weld was performed at 2 inches per minute for the 1500 RPM welds due to the poor performance at that traverse rate. The ultimate tensile strength of the welds increased with rotation and traverse speeds.
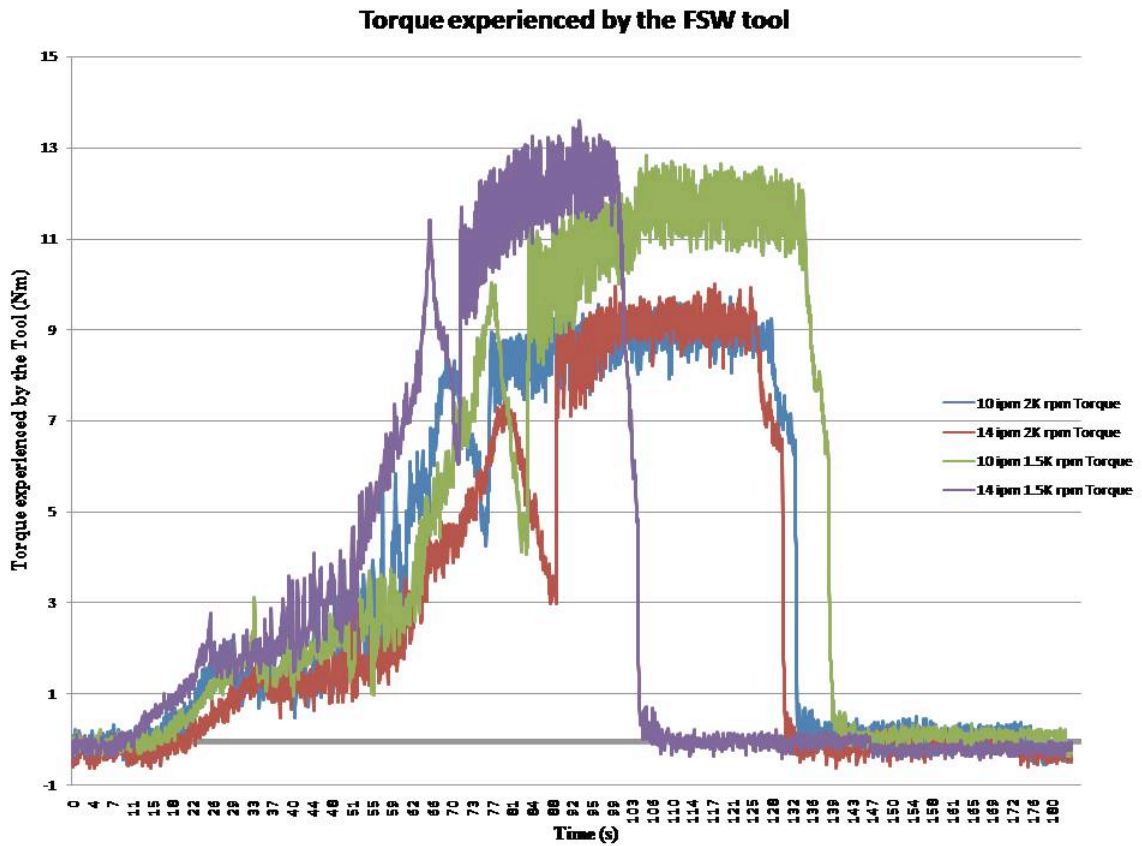
Figure 24: Weld torque for 1500 and 2000 RPMs at 10 and 14 inches per minute. X-axis represents the sample rate of the dynamometer during the weld (1 torque reading per second.)

The lower weld torques resulted in a reduced weld power, P (watts), according to the weld power model: where Ω (radians per second) is equal to the spindle speed and M (Nm) is equal to the weld torque:

$$P = Ω•M$$

The total heat input at the interface, Q, is defined as:

$$Q = P•β$$

where β (dimensionless) is the fraction of power dissipated by the tool into the weld material and the tool that is directly converted into heat. This β value is understood to be high. Santiago et al., [Santiago 2004], estimate this value to be 0.9 and De Vuyst et al. [De Vuyst 2007] quote a range of 0.9-1.0. Nandan et al. [Nandan 2008] refer to this (β) as the power efficiency factor, C_f.
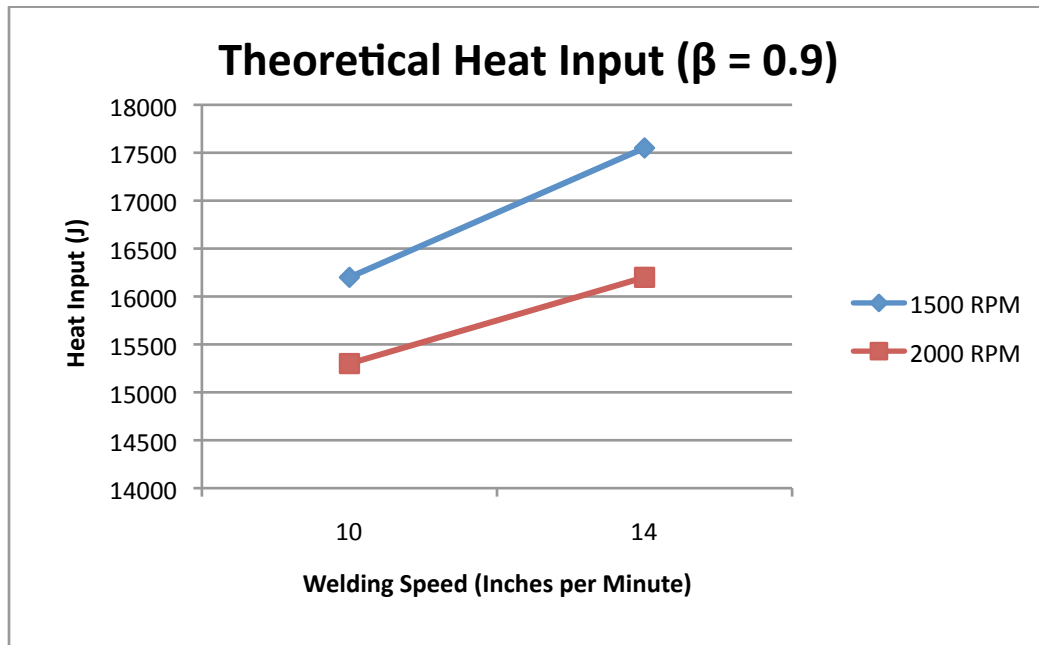
Figure 25: Plot of the theoretical heat input for different rotation and traverse speeds

Most assume this value to be 1.0 and define the weld efficiency simply as weld power minus the portion of the heat dissipated (0-10%) via conduction through the tool.

For this experiment it was observed that the 2000 rpm samples resulted in lower torque values than the 1500 rpm samples. Using the given expression for heat generation at the interface and the torque curves in Figure 24 the theoretical heat input to the weld was calculated and can be seen in Figure 25. The higher rpm welds had a lower calculated heat input at the interface. The lower torques associated with the higher RPMs

result in less total heat input at the tool/material interface, which is in good agreement with the results of Cao et al.

An increase in the traverse rate showed an increase in the calculated heat generation at the interface. However the function used to calculate the heat generation did not factor in the traverse speed of the weld. The measured torque was higher for the faster traverse rates but since the tool was in contact with the material for shorter amount of time (due to the increased traverse rate) the material was not exposed to as much heating. The results of Pareek et al. (see Figure 12) show that the grain size within the weld zone becomes more refined with an increase in the traverse and a decrease in rotation speed. The increase in ultimate tensile strength resulting from an increase in the traverse rate can be attributed to the decrease in the grain size within the weld due to the lower welding temperatures [Cao 2009].

Hammer Bend Test

The welds were subjected to another destructive mechanical test specifically developed to qualify the lap joint configuration. The Hammer Bend Test (see Figure 26) also known as an "S" bend test. A weld is said to successfully pass this test if the weld bends outside of the weld region without a crack propagating into the welded region. If a crack does propagate into the weld region the weld is said to fail this test. The parent material can crack, as is the case most often for the Mg, but as long as the weld does not crack the weld still passes the test. The results for the Hammer Bend Test can be seen in Figure 27.
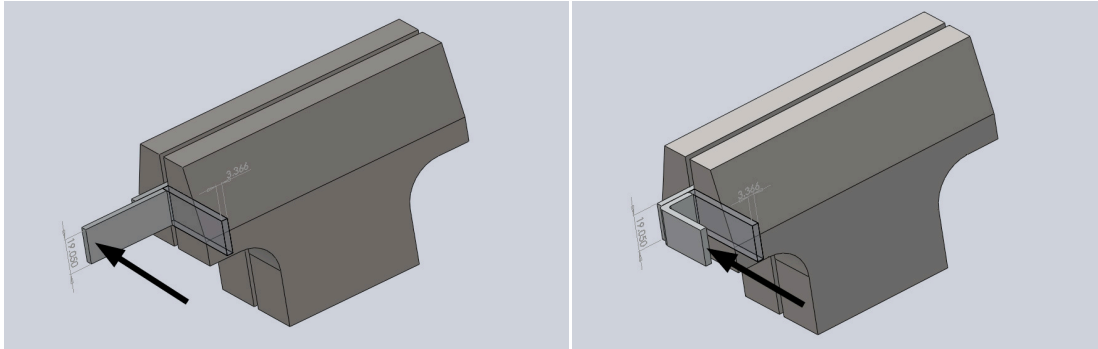
Figure 26: Left: Top plate of weld is clamped firmly while the bottom plate is struck in the direction of the arrow until a 90 degree bend occurs. Right: The bottom plate is now clamped firmly while the top plate is hit in the direction of the arrow until an "S" shape bend is achieved [Hendricks 2009].
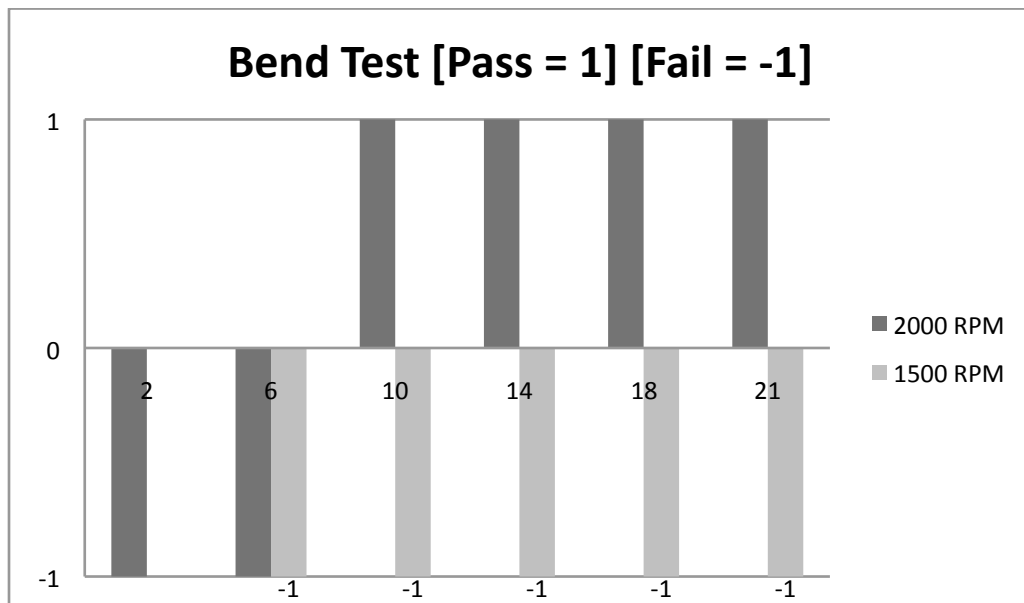
Figure 27: Results of the hammer bend test. Only the 2000 RPM welds passed this test.

Figure 27 uses a "1" to indicate successfully passing the test, and a "-1" to indicate failing the test. It can be seen that only the 2000 RPM welds successfully passed the Hammer Bend Test. It is also worth noting that only those welds at 10 inches per minute and higher passed the test for the 2000 RPM welds. The 10 inch per minute weld

had an average tensile strength of 63.70%, 10% stronger than that of the strongest 1500 RPM welds. The hammer bend test strongly correlated with the results of the tensile tests and was a good indicator of weld quality.

Surface features of the Welded Mg AZ31B

The physical appearance of the 2000 RPM welds can be seen in Figure 28. The sections of welds included in Figure 28 came from between the middle and end tensile coupons. In Figure 28 samples "b" and "c" did not have the coating removed. As previously mentioned the inclusion of this pickling layer in the weld has no appreciable effect on weld strength. The appearance of weld flash on "a" in Figure 28 did not occur for the entire length of the weld but was included to demonstrate some of the weld defects observed during the experiment. All of the 2000 RPM welds had no visual surface defects apart from the formation of "slight" weld flash which was caused by the non-uniformity in the thickness of the received materials.
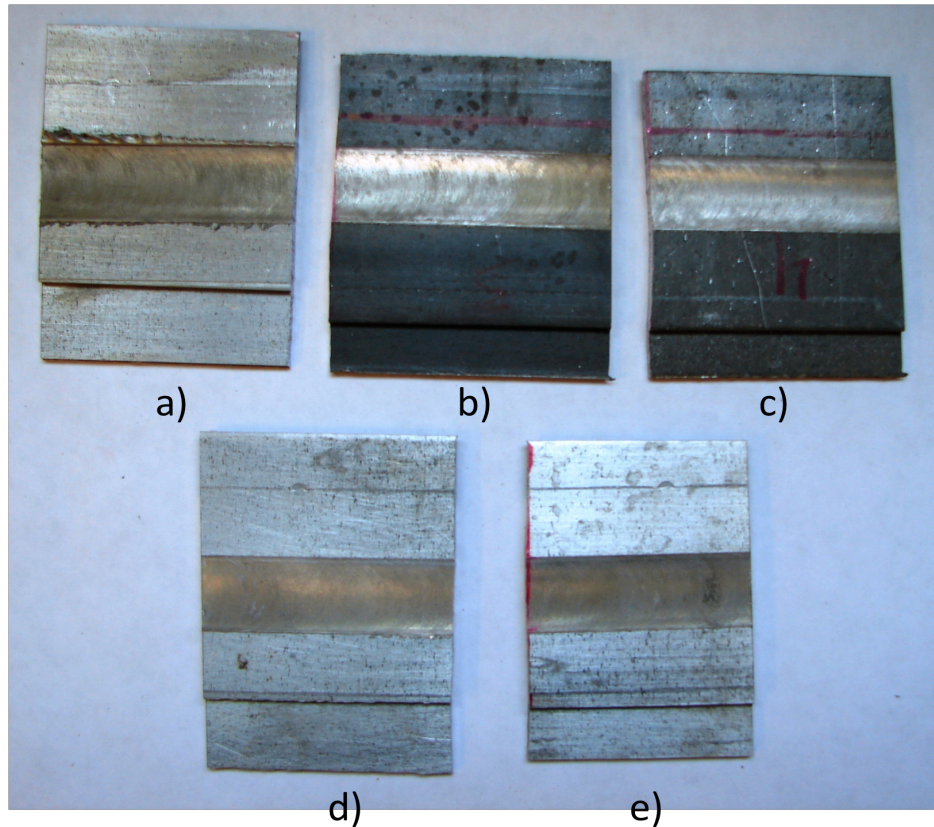
Figure 28 Photograph of the welds at 2000 RPM. a) 6 ipm b) 10 ipm c) 14 ipm d) 18 ipm e) 21 ipm

From Figure 28 it can be seen that the welds have no appreciable surface defects to indicate volumetric defects. The surface of the welds is smooth and even. However, to fully qualify the welds interior inspection of the weld must be performed to check for voids such as fissures and worm holes, or other related weld flaws/defects. To perform these analysis sections of the weld were removed for metallurgical analysis.

Cross Sections of the Welded Mg AZ31B

The weld sections were taken from between the middle and last tensile coupons (see Figure 20), the same locations as those from Figure 28. The samples were then cut and trimmed to approximately the size of the weld zone (TMAZ) and a portion of the parent material on both the retreating and advancing sides of the weld. All of the cross sections were taken to have the advancing side to the left and the retreating side to the right when looking at the weld with the weld surface being on the top (see Figure 16). The samples were cut with a wet saw using a diamond tipped saw blade in order to produce a clean metal surface for polishing (see Figure 29).
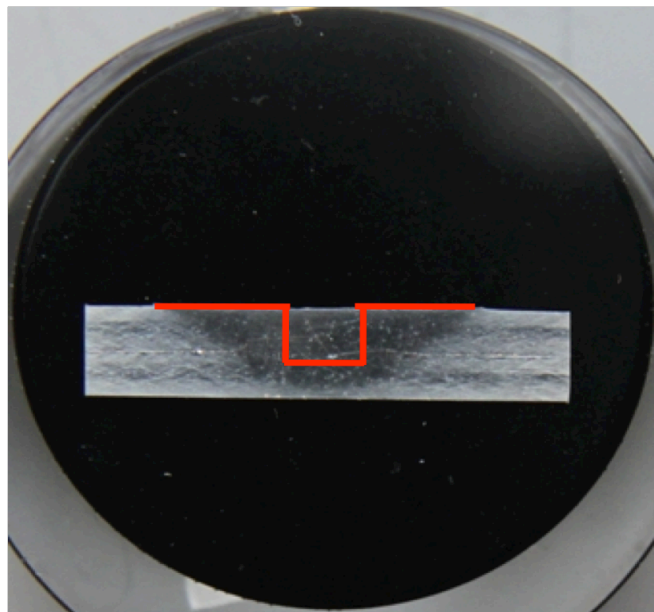
Figure 29 Mounted sample of AZ31B etched to relieve weld zone. Also shown is a graphical representation of the tool profile with relation to the weld zone.

Once cut, samples were hot mounted into black resin pucks. These resin pucks make it easier to handle the sample for polishing, etching, and imaging. Once mounted the samples were polished using increasingly finer polishing paper until a mirror like finish

appeared in the metal. The samples were then etched with dilute acetic acid in order to make the weld zone visible. The samples were imaged at both low resolution (1x) and high resolution (10x) to help see the weld zone and any defects that were present.
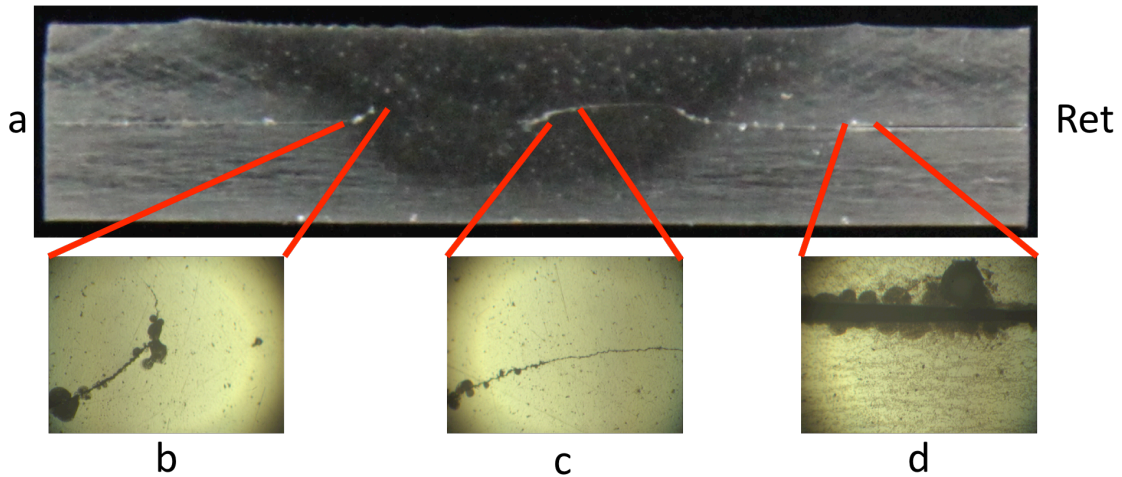
Figure 30 Weld 10: 18 ipm 1500 rpm 55% parent UTS, a) 1x image of weld zone b) 10x view of hooking defect on advancing side c) 10x view of joint line remnant within weld zone, d) 10x view of gap between parent plates (unwelded)

Weld 10, which had the as received coating removed before welding, is shown in Figure 30. The weld zone is uniform and shows good integration between the top and bottom plates. However, this weld did have volumetric defects that may be a cause of the low tensile strength. Image "b" in Figure 30 shows a hooking defect on the advancing side of the weld. It can also be seen that a joint line remnant (JLR) exists for approximately 50% of the weld (see Figure 2 of the Appendix for a sketch of the hooking defect). The occurrence of this flaw only appears on the retreating side of the weld where the material is beginning to be being deposited. This JLR is significantly smaller than the gap between the plates of the unwelded material. This line is also accentuated by the oxide layers occurring at the boundary between the two plates and the etchant used to bring out the

weld zone. The material within the weld zone (Figure 30 "b" and "c") also has a much smoother appearance than that of the material outside of the weld zone (Figure 30 "d") indicating that the material of both plates in the weld zone experienced to some extent uniform heating/plastic deformation. Meaning the two plates in the weld zone are indistinguishable.
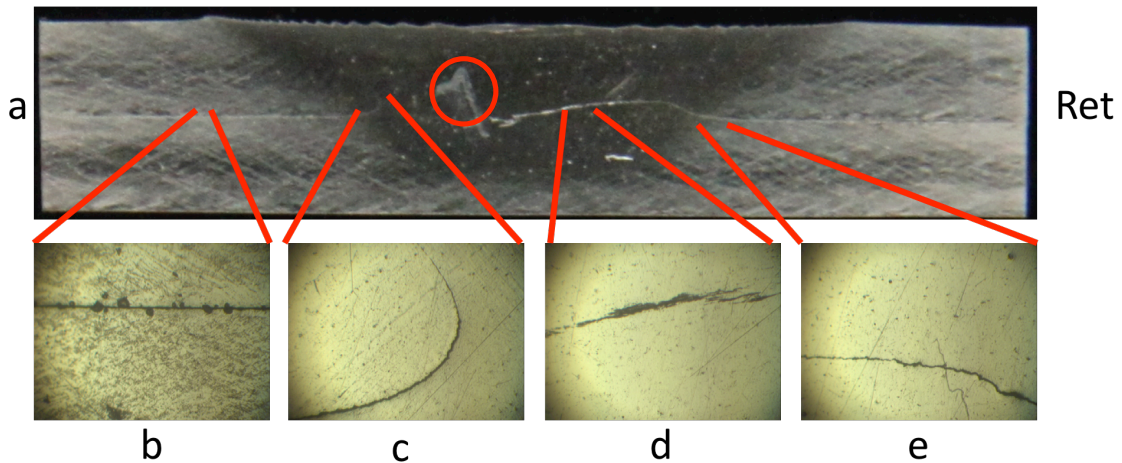
Figure 31 Weld 11: 21 ipm 1500 rpm 52% parent UTS, a) 1x image of weld zone b) 10x view of gap between parent plates (unwelded) c) 10x view of hooking defect on advancing side d) 10x view of joint line remnant within weld zone, e) 10x view of the interface between the weld zone joint line remnant and the gap between the parent plates

Weld 11, which had the as received coating removed before welding, is shown in Figure 31. The weld zone is uniform through both the top and bottom plates. Figure 31 "c" shows the hooking defect on the advancing side of the weld similar to that of weld 10. The JLR as shown in Figure 31 "d" is similar to that of weld 10, but is not a continuous line, and also occurs on the retreating side of the weld. Figure 31 "d" shows the discontinuity of the joint line remnant. There is a large weld flaw seen in Figure 31 "a" (circled) that appears to be a collection of oxides to the left of the weld path. Again the

weld zone has a distinct uniformity between the top and bottom plates that is not seen

outside of the weld zone.

Figure 32 Weld 1: 10 ipm 2000 rpm 65% parent UTS, a) 1x image of weld zone, b) 10x view of the hooking defect on the advancing side of the weld, c) 10x view of material within the weld zone, d) 10x view of joint line remnant within the weld zone, e) 10x view of gap between parent plates (unwelded)

Weld 1, which did not have the as received coating removed before welding, is shown in

Figure 32. The effects of the inclusion of this coating can be seen in the Figure. The

bright areas on the bottom and top of Figure 32 "a" are the results of this layer. The

effects are also noticeable at the interface between the top and bottom plates. The size of

the JLR is slightly larger due to the increased quantity of the oxide/coating layer. The

difference between the JLR and the gap between the top and bottom plates can be seen in

Figure 32 "d" and "e". The JLR is less formed with more non-uniformity along its length.

The hooking defect occurred for this sample along the advancing side of the weld, the

same as that of the 1500 rpm welds. Weld flash can be seen on both the advancing and

retreating sides of this weld which indicates that the plunge depth placed too much of the

shoulder beneath the surface of the weld. This can lead to volumetric voids within the

weld. In this case no volumetric voids were detected.
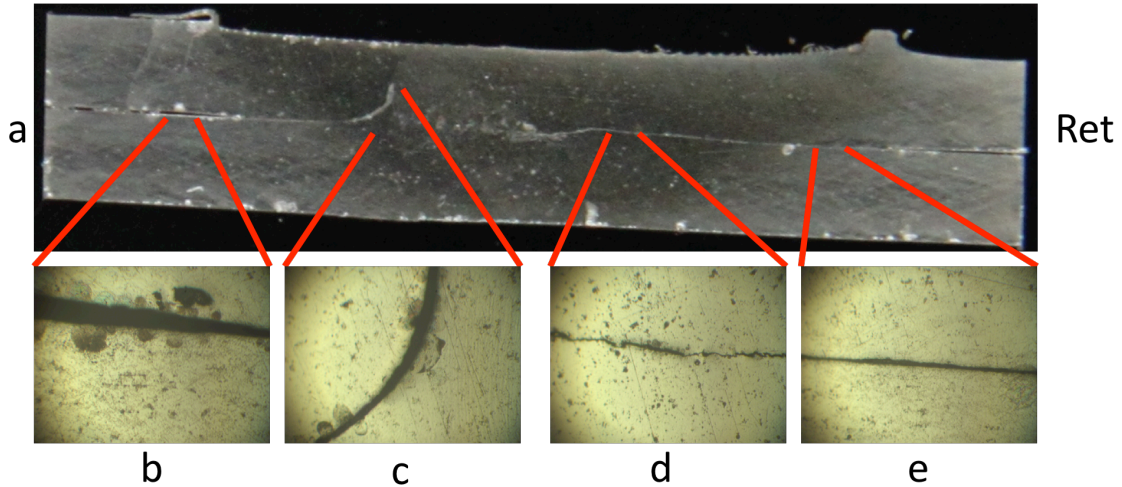
Figure 33 Weld 2: 14 ipm 2000 rpm 85% parent UTS, a) 1x image of weld zone, b) 10x view of gap between parent plates (advancing), c) 10x view of the hooking defect on the advancing side, d) 10x view of joint line remnant within the weld zone, e) 10x view of gap between parent plates (retreating)

Weld 2, which did not have the as received coating removed before welding, is shown in

Figure 33. Weld flash is again visible on both sides of the weld for this sample. The

increased plunge depth resulted in an apparent increase in axial loading evidenced by the

increase in gap size between the unwelded portions of the top and bottom plates.

However there were no observed volumetric defects for this sample. A hooking defect

was seen in this weld along the advancing side of the weld though this weld successfully

passed the hammer bend test. The JLR was also seen on the retreating side of the weld

zone but was considerably less uniform than that of the gap between the unwelded zones.
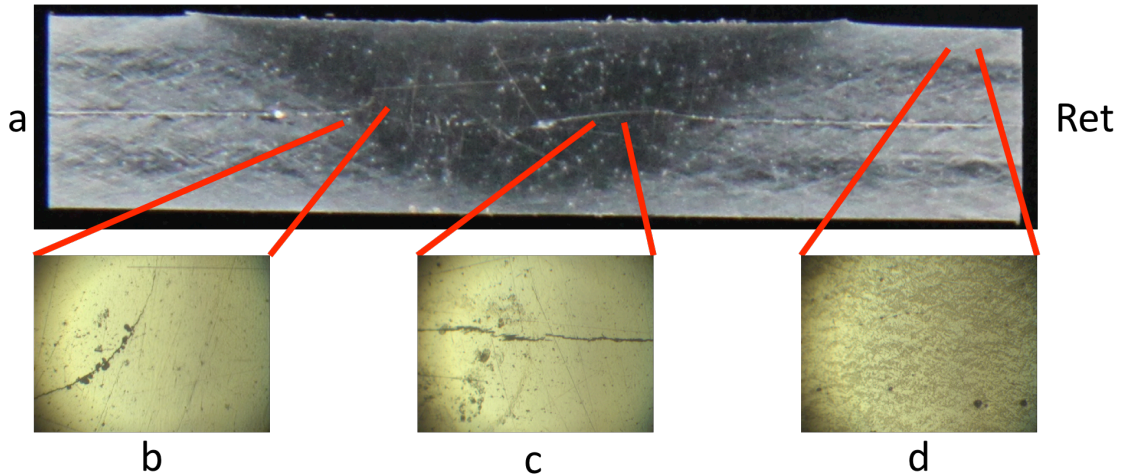
Figure 34 Weld 7: 18 ipm 2000 rpm 87% parent UTS, a) 1x image of weld zone, b) 10x view of the observed hooking defect (advancing), c) 10x view of joint line remnant within the weld zone d) 10x view of parent material

Weld 7 can be seen in Figure 34. This is the strongest weld from the study. The appearance of the hooking defect is again observed to be on the advancing side of the weld. Also, the JLR is again observed on the retreating side of the weld. In this case Figure 34 "b" shows the discontinuities of the joint line. Further, the hooking defect observed is much less significant. Figure 34 "d" captures the appearance of the unwelded/unaffected material for comparison to that of the material in the weld zone. This sample had no appreciable formation of weld flash and no volumetric flaws/defects.
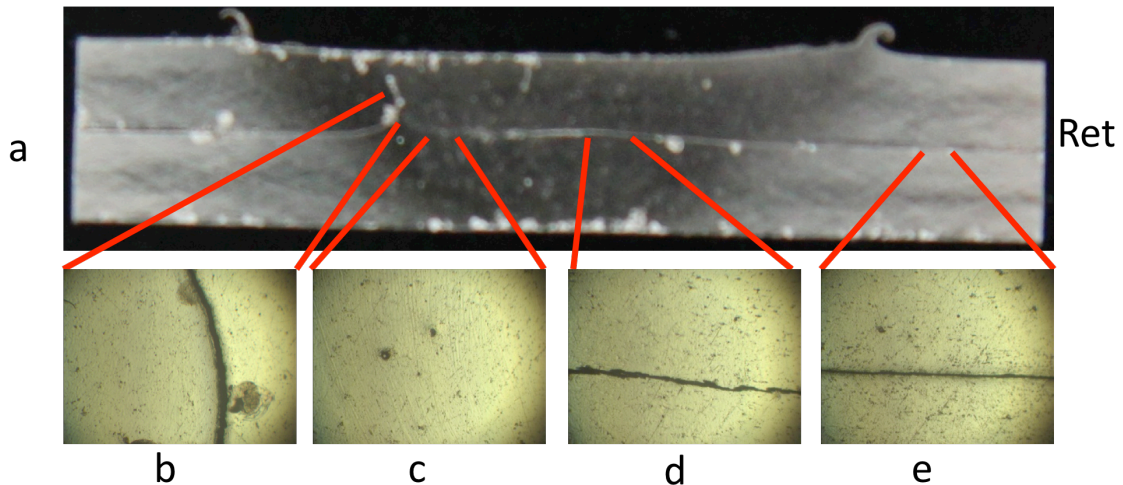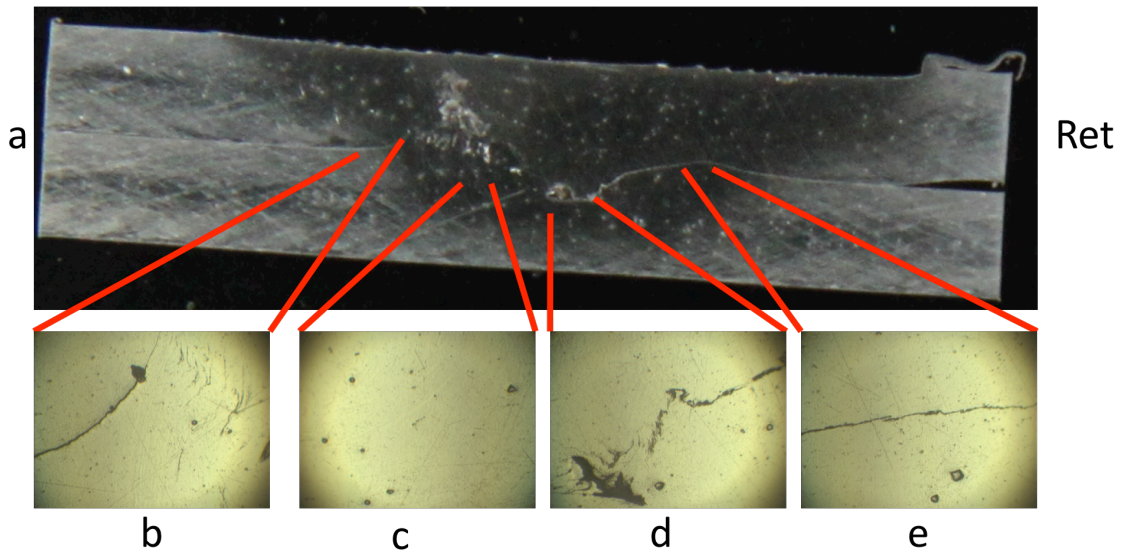
Figure 35 Weld 8: 21 ipm 2000 rpm 86% parent UTS, a) 1x image of weld zone, b) 10x view of the observed hooking defect (advancing), c) 10x view of the material within the welded zone d) 10x view of joint line remnant within the weld zone and volumetric weld flaw e) 10x view of joint line remnant within the weld zone

Weld 8 can be seen in Figure 35. There was a hooking defect on the advancing side of the weld. Within the welded zone, Figure 35 "c", there is significant mixing between the top and bottom plate; there was no visible JLR. Figure 35 "d" shows a volumetric defect within the middle of the weld path. The JLR, Figure 35 "d" and "e" show the discontinuities within the joint line. Weld 8 was the second strongest weld in this study. This weld also passed the hammer bend test. There was some observable flash on the retreating side of the weld which resulted in a larger gap between the unwelded portions of the top and bottom plates on the retreating side.

Each of these welds were chosen to provide examples of what made the weld joint significantly stronger or weaker than the other welds in the study. Weld numbers 10 and

11 were the strongest of the 1500 rpm welds but failed the hammer bend test. These welds also only tested for a tensile strength of a maximum 55%. Upon initial observation the weld surface was smooth, uniform, and showed no sign of surface defects or flaws. However, when cross sectioned it was seen that both of these welds contained hooking defects along the advancing side of the weld. Also, the weld zones of these samples showed joint line remnants that were "shifted" upward (in relation to the cross section). This shift upward seems to be related to a possible lack of stirring in the downward vertical direction near the pin surface. With the lower rotation speed of these samples, when compared to the 2000 rpm welds, the results of the tensile experiments are in agreement with the cross section evaluations. However, these welds (10 and 11) failed each of the mechanical tests at the interface between the top plate and weld zone on the advancing side and not on the retreating side where the JLR was present.

It was observed that each of the cross sectioned welds (Figures 30, 31, 32, 33, 34, 35) contained small (white in appearance) particles within the weld zone. It is thought that these particles are similar to the dispersoids observed by Pareek et al. However no analysis was performed to determine the exact chemical composition of the particles, but they are similar in appearance and size to the results of Pareek et al. The inclusion of the dispersoids within the weld zone has no affect on the tensile strength of the welds [Pareek 2007]. Also the observance of these particles did not tend to favor the advancing side over the retreating side as seen in the results of Pareek et al.

The remaining weld samples that were cross sectioned were chosen based upon their higher tensile strengths and their passing the hammer bend test. Weld 1 had the lowest tensile strength for a weld that successfully passed the hammer bend test. From

46

this, the hammer bend test could be used as a reasonable indicator of weld strength. Further, the hammer bend test requires less time and resources to complete making it an even better candidate for a cursory examination of weld strength. Welds 2, 7, and 8 all exhibited excellent weld strength at over 85% of the parent material strength. Each of these welds (all at 2000 rpm) had hooking defects on the advancing side and JLR s on the retreating, similar to that of the 1500 rpm weld samples. The JLR for these welds was observed to have been displaced in a downward direction from the original joint line interface. This downward displacement, especially near the pin, could be attributed to the increased material flow caused by the threaded pin and the increased rotational velocity. Each of these welds fractured outside of the weld zone during the tensile tests.

The effect of the presence of the JLR and hooking defect within the weld zones on tensile strength is unclear. Each weld in the study exhibited, to some extent, the presence of both of these defects. Typically the presence of these defects, or voids, severely reduces the strength of the weld joint. However welds 1, 2, 7, and 8 all exhibited good tensile properties (65-87%).
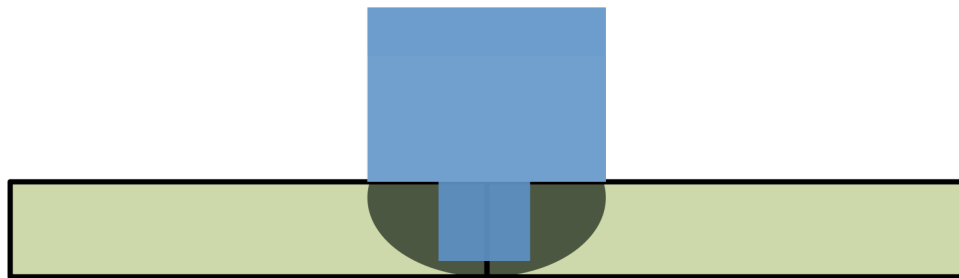
Figure 36 Graphical representation of a typical full penetration butt weld joint configuration

One possible explanation for the significant presence of the JLR seen in the lap welded Mg AZ31B could be attributed to the joint configuration itself. The typical butt joint weld configuration can be seen in Figure 36. The tool is represented by the blue object, the material by the green rectangles, and the TMAZ by the dark semi-circle. The welding direction is into the page. For this weld, the joint line is completely mechanically disrupted by the pin. If any JLR remains it would be dislocated to the outer edge of the weld zone. Further, the presence of oxide layers between the plates is minimal as the surface area of the material joint line is significantly small. If there is a presence of the JLR it can be reduced by increasing the length of the pin, effectively mechanically displacing more of the original joint line.
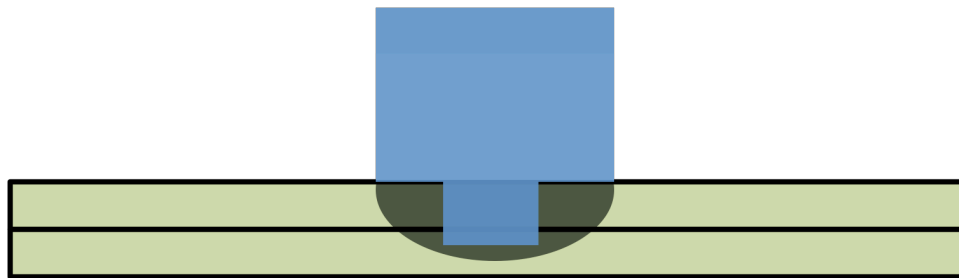
Figure 37 Graphical representation of a typical lap weld joint configuration

When considering the lap joint weld configuration it can be seen that the joint line extends for the entire length of the material perpendicular to the weld line. The typical geometry of a lap joint can be seen in Figure 37. For this geometry the pin of the tool only directly mechanically displaces the portion of the joint line that overlaps with the weld path, meaning that the stirring must take place through the rigid interface created by the top and bottom plates. Further, the presence of oxides is significantly higher for this geometry, several times over that of the butt weld, which was clearly observed in the

cross sections of the weld samples. Increasing the length of the pin is not a reasonable way to eliminate the JLR (as is the case for butt joints) since it will not help increase the amount of the joint line being mechanically affected. Instead the pin would need to have its diameter increased. However, increasing the pin diameter would require that the diameter of the tool shoulder be increased to maintain a proper pin to shoulder ratio. A better option to eliminate, or at least reduce, the presence of the JLR would be to: a) use a tool with a higher static to swept volume ratio such as the A-skew^{TM} tool design (see Table 1), b) use a weave-type weld path to increase the width of the weld nugget c) some combination of a and b. Increasing the width of the weld zone would help reduce the presence of the JLR.

The observed JLR is also reported by Cao et al. in their 2009 publication. Termed the "kissing bond", the boundary between the top and bottom plate throughout the weld zone was characterized by Cao as having irregular morphologies which they attributed to the oscillating welding forces of the process. Moreover, Cao et al. determined that these "kissing bonds" are formations of oxide bands which are typical for welding Mg alloys. It also stated that the width of a kissing bond is much narrower than that of a hooking defect but can be detrimental to the tensile strength of a weld [Cao 2009]. The presence of the joint line remnant does not affect the tensile properties of the weld [Kumar 2010].

The tool used in this study did however provide sufficient stirring and material flow (see Figure 38).
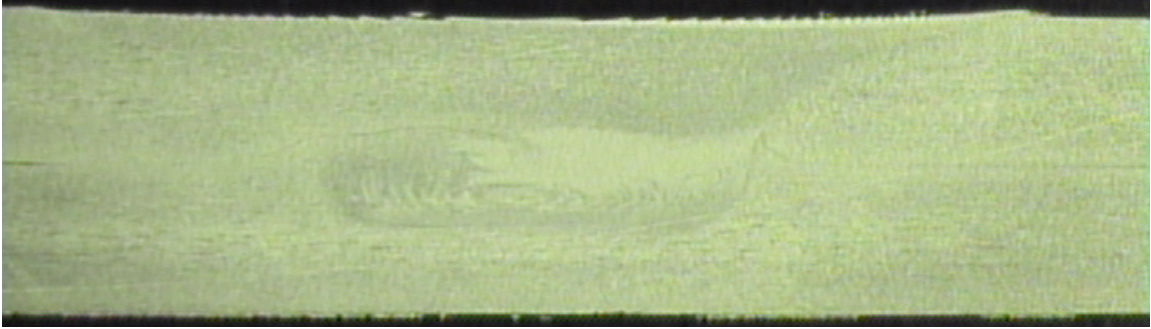
Figure 38 Weld 3 10 ipm, 1500 rpm, 55% UTS of parent material, non-etched. Retreating side is to the left of the image, advancing to the right.

In Figure 38 it can be seen that there was sufficient stirring at the bottom of the weld and throughout the weld zone. JLR can be seen on the retreating side and a slight hooking defect is visible on the right outside of the weld zone.

Summary of Experimental Lap Weld Results

- It has been demonstrated that friction stir welding is a viable method for joining Mg AZ31B H24 in a lap joint configuration with a single pass.
- Welding forces were significantly higher (100%) for Mg AZ31B than for Al 6061 T6.
- Higher rotation speeds increased the overall tensile strength of the welds by increasing the stirring.
- Increasing the traverse speed increased the overall tensile strength of the welds; or rather colder welds increased the tensile strength of the welds.

- The results of this experiment are the highest reported tensile strength for Mg AZ31B lap welds, 87% parent strength, 35% stronger than previously reported by Cao et al.

- The results are also on the same level as the highest reported % parent strength of butt joint welds, 85% parent strength by Lee, et al.

CHAPTER IV

A CFD MODEL FOR THE FRICTION STIR WELDING OF Mg AZ31B

Introduction

To gain better understanding of the processes present during the friction stir welding of Mg AZ31B a computational fluid dynamics model (CFD) of the process was created. The use and application of CFD for FSW is a widely accepted method of modeling as previously published by Cox et al. (2010), Lammlein et al. (2009, 2010), Sinclair et al. (2009), and Crawford et al. (2006). Each of these models from the Vanderbilt University Welding Automation Laboratory were created to either predict the effects of specific variable changes in the process or to help explain an observation that was unexpected or not well understood. CFD models of FSW provide the users with information regarding temperature and velocity profiles of the welded material and tool and to some extent the axial loading on the tool during welding. While the prediction of forces is not as directly comparable to the actual process, general trends and behaviors have been predicted with the models. However there are some differences between the previously created models and that of the model used for the purposes of this study.

The aforementioned models dealt strictly with an aluminum alloy (Al 6061 T6) using steel tools with smooth pins, conical pins, and threaded pins. The model created for this study has two distinct differences: a) the material modeled is a magnesium alloy (Mg

AZ31B) which has been discussed very little in recent publications b) the tool used for

the experiment has threads, flutes, and a cupped tip which makes the creation of the mesh

slightly more involved. The description and results of the model will be described.

Creating the Mg AZ31B CFD Model

The model was created using a commercially available CFD software package

called FLUENT created by the company Ansys. FLUENT was the software package used

for the previously mentioned CFD models. FLUENT is a general CFD code based on the

finite volume method located on a collocated grid or mesh. While FLUENT is used to

handle the simulation of the process, Gambit (also created by Ansys) allows the user to

import a design from another CAD program or can be used to create the geometries,

boundaries, grids, and meshes for the model; the latter was used for this study.

Tool Geometry and Mesh

The tool used for this experiment is a modified tri-flute design. The 3D geometry

of the tool pin can be seen in Figure 39.
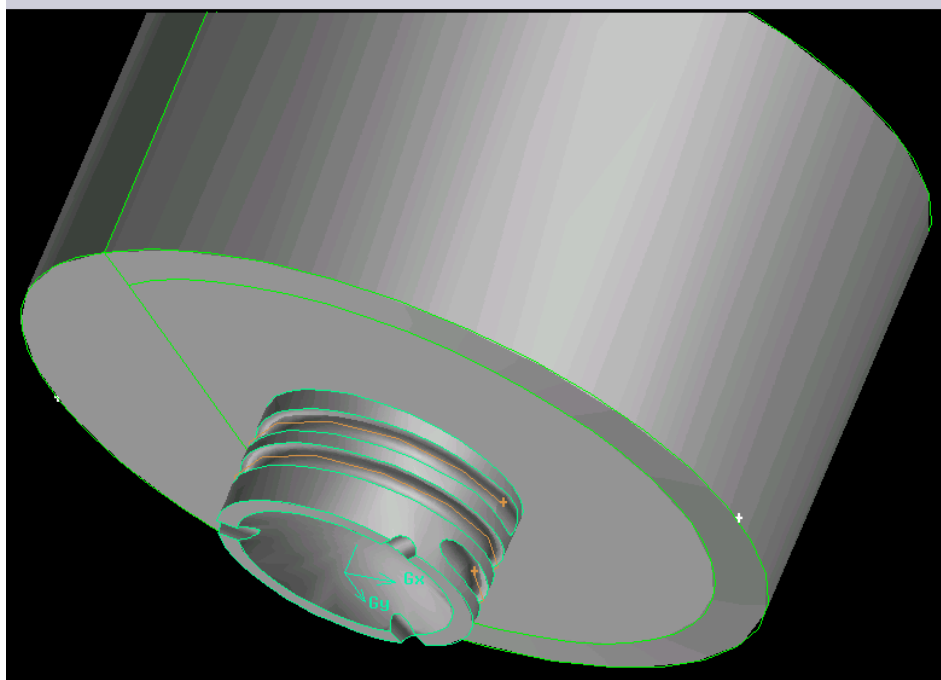
Figure 39 3D geometry of the tool pin created using Gambit. The tool is threaded, has 3 notches in a triangular orientation, and a cupped tip.

a

b
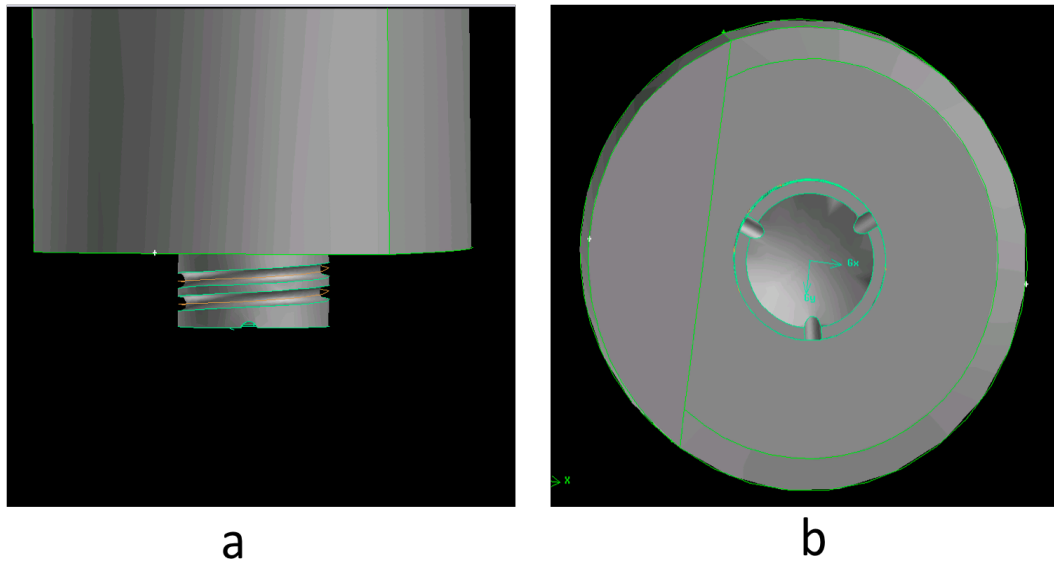
Figure 40 a) CFD tool pin vertical profile b) CFD tool pin horizontal profile (bottom - up)

The tool was created to have the same overall physical dimensions and similar characteristics as the tool used for the experimental section. The tool has a shoulder diameter of 0.625 in, a pin diameter of 0.250 in, and a pin length of 0.116 in. Only a portion of the plate was modeled (3" x 6") since only a small area is mechanically affected. The thermal boundaries were handled via boundary conditions (conduction, heat flux, fixed temperatures, etc.) The plates were modeled as a continuous plate without the rigid boundary inherent with the lap welds.

Once the geometries for the FSW tool and material samples were created Gambit was used to create the three dimensional mesh/grid that FLUENT will use to solve the CFD model. The mesh was created to have more nodes and therefore more refinement around the areas of interest (the tool pin, shoulder, and probe bottom.) The choice of increased mesh refinement largely parallels areas of the geometry with finer details. A tetrahedral type volumetric element was used for the entire model. The tool consisted of 43,188 nodes and 234,100 elements. The material plate consisted of 77,737 nodes and 419,614 elements. The minimum skewness for an element within the model was 1×10^{-6} and the maximum skewness was 0.749. Skewness is a measure that describes the aspect ratios for the elements in the model and a skewness of greater than 0.75 is not wanted. Only one element in the model had a skewness of 0.749.
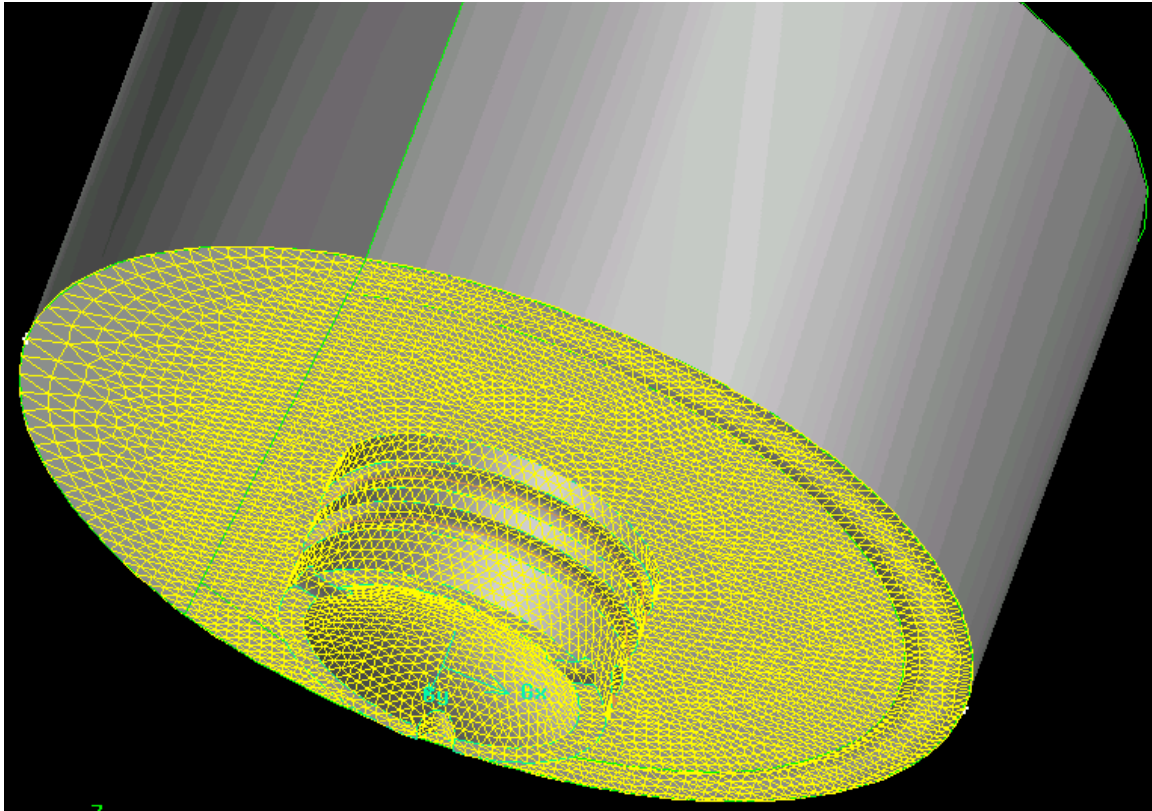
Figure 41 Mesh of the shoulder and tool pin. The left (in the image) side of the shoulder has a visibly larger mesh size since it is not in direct contact with the material.

From Figure 41 it can be seen that the mesh size is more refined for the pin (and threads) than for the rest of the tool. This is because (as previously stated) the pin in directly in contact with the material that is being mechanically displaced and has the highest level of geometrical intricacy (threads, flutes, cups). Figure 42 shows a closer view of the tool meshing.
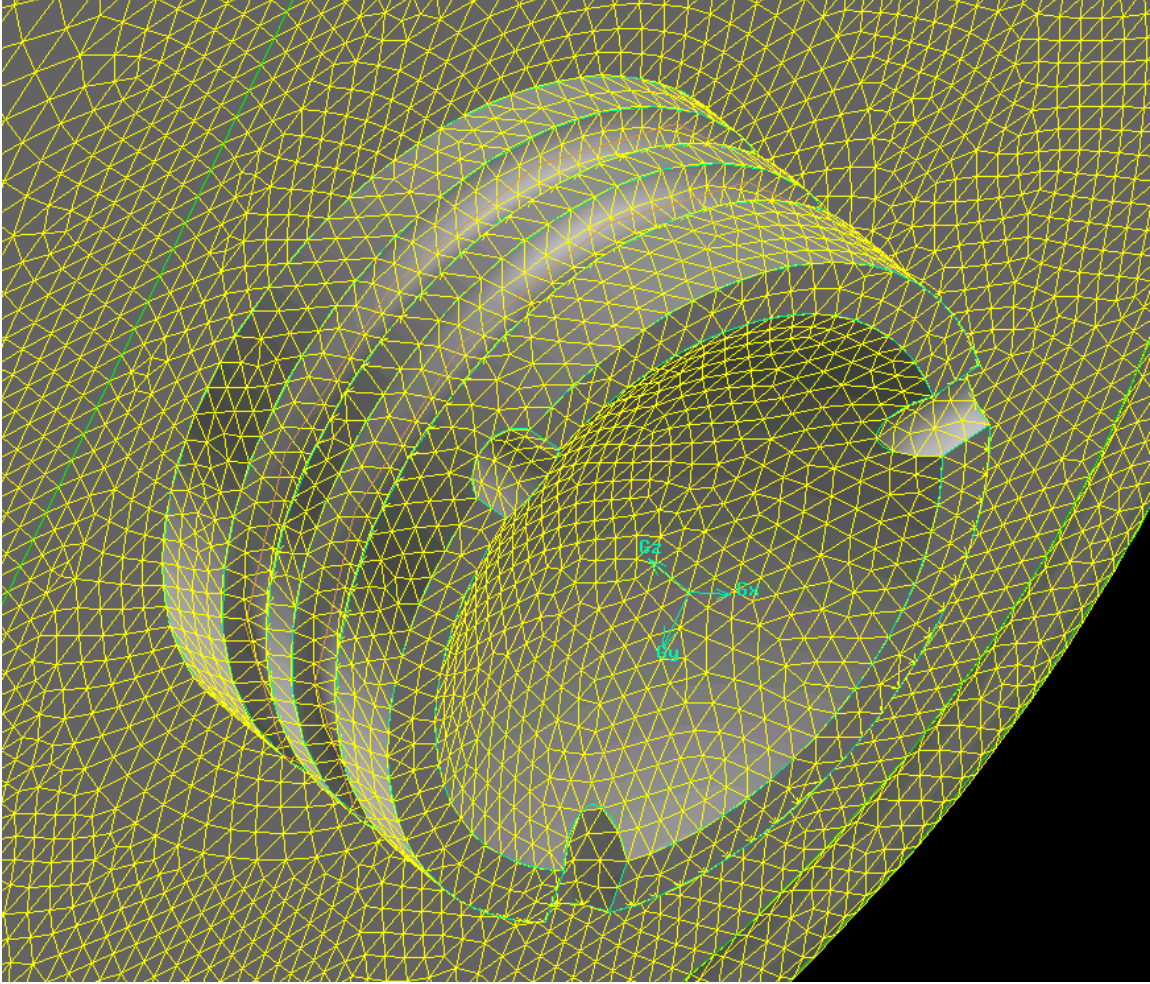
Figure 42 Close-up view of the meshing used for the tool

Figure 42 better shows the distinction between mesh refinements for areas of the tool. It can be seen that there is significant difference between the mesh size used for the interface between the threads and the cup, the pin and the shoulder, and the shoulder section located at the top left of the image. A refined mesh could be used for the entire model but would drastically increase the run time without providing a better or more accurate solution. Figure 43 provides a look at the meshing used for the entire model.
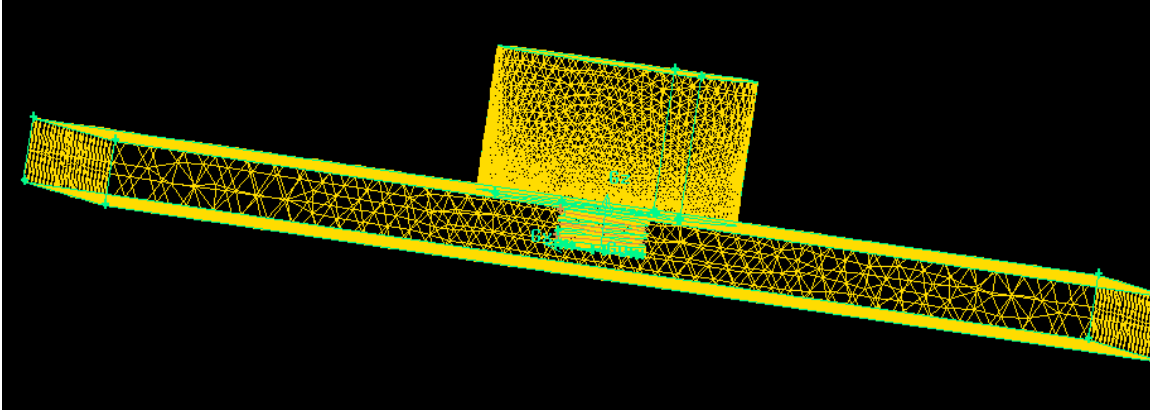
Figure 43 Complete mesh used for the model

Again, one can be see the differences in mesh refinement between the tool and the plate. In Figure 43 the mesh used for the shoulder, plate, and pin can be seen. There are fewer nodes in use on the side walls of the plate than that of the pin and shoulder due to the lack of rapid mechanical and thermal activity at these boundaries.

Boundary Conditions

The boundary conditions for this model can be seen in Figure 44. The tool itself was modeled as a single solid mass. To model the thermal effects of the tool shank, tool holder, and heat transfer up through the spindle a specific heat transfer coefficient was used. A coefficient of 100 W/m^2K was used for the top of the tool and a coefficient of 30 W/m^2K was used for the sides of the tool. The heat input through the interface between the shoulder and the material were modeled as a heat flux which was adjusted to agree with the observed experimental torque values. The top surface of the plate was given a convective heat transfer coefficient of 20 W/m^2K and the bottom surface of the plate was given a conductive heat transfer coefficient of 100 W/m^2K. The top of the plate interfaces

with the ambient air while the back of the plate is in contact with a large thermal mass. The "fresh" material was set to be 300°K while the exit was modeled as a pressure outlet. The rotation of the tool was modeled by setting the velocities of the walls representing the pin, shoulder, and the bottom of the pin as having a local tangential velocity about the central axis of the tool (tilted 1° relative to the coordinate from of the model.)

Tool Shank k = 100 W/m²K

Convective heat transfer coefficient = 30 W/m²K

Total Heat Input at Tool Surface = 1010 Watts

Convective heat transfer coefficient = 20 W/m²K

T = 300K

FSW Tool

Velocity Inlet

Pressure Outlet

Magnesium Plate

Tool Traverse Direction

Steel Backing Plate

Backing Plate k = 100 W/m²K
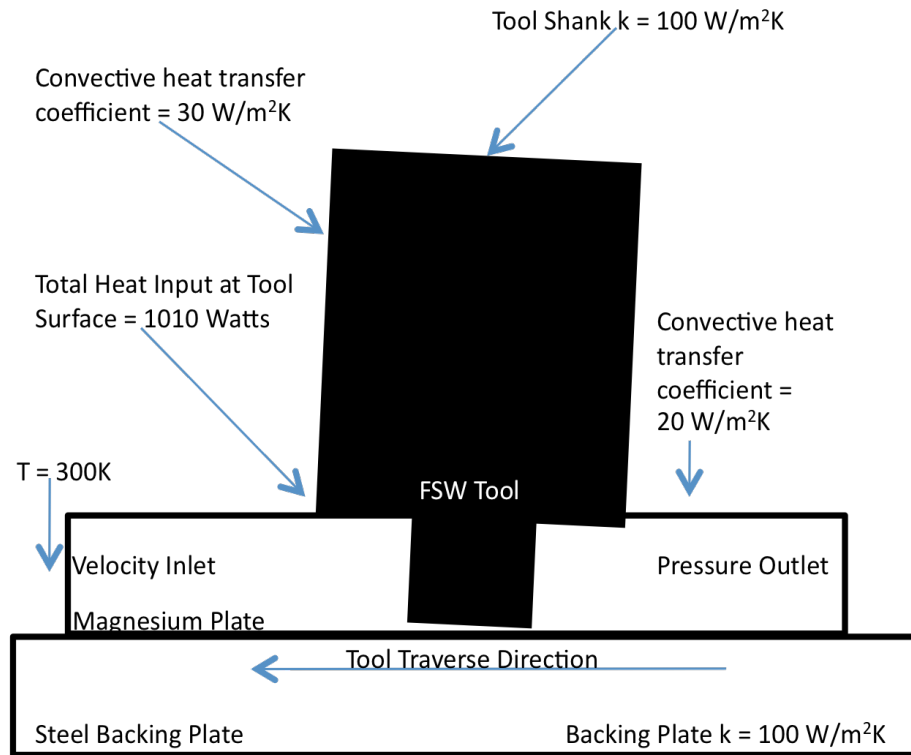
Figure 44 Boundary conditions used for the CFD model of the FSW of Mg (graphical representation).

CFD Model for FSW of Mg AZ31B

The CFD model was created using the Eulerian, finite volume, CFD solver, FLUENT. The mechanically affected zone is modeled as having a viscosity, which can be approximated using the visco-plastic model modified by Sellars and Tegart, a widely

used model [Sellars 1966]. The flow stress, as defined by Sellars et al., appears as the following expression:

$$\dot{\varepsilon} = A[\sinh(\frac{\sigma}{\sigma_R})]^n \exp(\frac{-Q}{RT})$$

Where A (s^{-1}), n, σ_R (MPa) (effective stress), and Q (kJ mol^{-1}), the activation energy, are all defined to be material constants determined from curve fitting experimentally obtained data with the Sellars and Tegart formulation [Tello 2010]. The effective stress (σ_R) is sometimes expressed as alpha (α (1/MPa)) and is obtained from curve fitting experimental data. The effective stress (also known as the von Mises stress) is a scalar value that measures the intensity of the entire stress state as it includes the three principal stresses in the x, y, and z directions, along with the shear stresses on the x, y, and z planes [Logan 2007]. R is the universal gas constant and T is the reference temperature (°K).The results of their work can be seen in Figure 45. This expression is similar to the calculation used for the Zener-Holloman parameter. For example, re-writing the Zener-Holloman parameter using the Sellars formulation for strain rate yields a similar relationship relating stress with the activation energy and temperature, which helps to characterize dynamic recrystallization [Pareek 2007].

$$Z = A[\sinh(\frac{\sigma}{\sigma_R})]^n$$

Substituting this expression back into the Sellars formulation of strain rate yields (another form of the Sellars and Tegart expression used in the literature):

$$\dot{\varepsilon} = Z \exp(\frac{-Q}{RT})$$
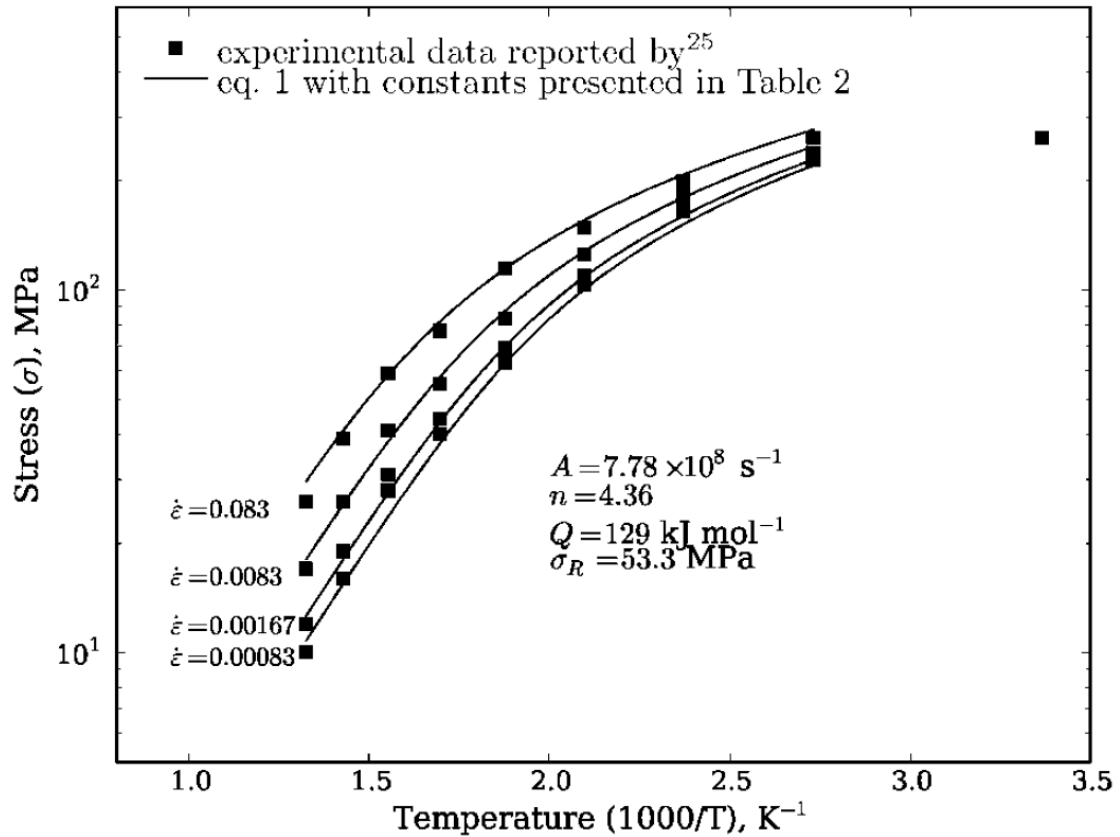
Figure 45 Hot deformation data for Mg AZ31B (temperature range is approximately 350 - 715°K) [Tello 2010]

The values used for the expression can be seen in Figure 45 (A = 7.78×10^8 s^{-1}, n = 4.36, Q = 129 kJ mol^{-1}, σ_R = 53.3 MPa).

FLUENT requires that the material being modeled have a defined viscosity. Colegrove et al. approximated the viscosity (μ) of the metal using a ratio of the effective stress and the strain rate [Colegrove 2005] (see Figure 3 of the Appendix for the user defined function (UDF) used to approximate the viscosity in FLUENT):

$$\mu = \frac{\sigma_R}{3\dot{\varepsilon}}$$

As the metal approaches the melting temperature significant softening occurs which reduces the amount of additional energy needed for plastic deformation. Mg AZ31B's temperature dependent properties were listed and discussed in an earlier section (page 10 of this thesis). The total heat input was calculated using the weld power method as previously discussed (page 33 of this thesis). However for review the expression for weld power has the form:

$$P = \Omega \bullet M$$

The total heat input at the interface, Q, is defined as:

$$Q = P \bullet \beta$$

Where P is the weld power (W), Q is the heat input (W), Ω is the tool rotation speed (rad/s), M is the observed torque (N•m), and β represents the fraction of heat transmitted into the weld. The rotation speed was set to 70% of the experimental value 2000 rpm's. The feed rate for the model was 10 inches per minute. The viscosity, density, and rotation (spindle) speed were increased iteratively in order to reach a sound and converged model.

Results and Discussion of the CFD Model

The results of the model are in good agreement with, and help explain the experimental observations. The model was used to observe the heat transfer and material flow within the weld zone. The highest temperature reported in the model was around 600°C and occurred within the geometry of the tool. This is slightly higher than the experimentally observed, though the experimental observation was made higher up the shank of the tool

62

using thermal imaging equipment (the experimental observation from the shank is in good agreement with the temperature of the shank from the model, approx. 530°C). These temperatures are below the melting point of Mg AZ31B.

Figure 46 Static temperatures found within the weld zone. The cross section view is taken halfway through the vertical tool plane. The advancing side is to the left of the tool.

From Figure 46 it can be seen that the advancing side of the tool is significantly hotter over a larger percentage of the area than that of the retreating side. This difference in temperature most likely stems from the removal (resistance) of material from the advancing side and the deposition of the material on the retreating side. The lower temperatures on the retreating side provide a better picture as to why the joint line

remnant only appears on the retreating side of the pin. The appearance of the joint line remnant typically suggests that there is insufficient stirring from the pin, and therefore the oxide layer is not able to be completely broken up by the tool. From this we can see that the lower temperatures on the retreating side can be related to the observed presence of the joint line remnant in each of the welds that were cross sectioned. These results are in agreement with Kumar et al. which found that it is on the advancing side that the material begins undergoing plastic deformation. Having this initial interface on the advancing side avoided the formation of the joint line remnant [Kumar 2010].

The higher temperatures on the advancing side are above the solidus point (605° C) for Mg AZ31B. At this temperature the metal begins to soften but it not completely melted making it easier for the metal to plastically deform. The advancing side of the tool is mostly above this temperature while the retreating side of the tool is mostly below. The higher temperatures on the advancing side indicate that the material on this side is significantly softer which would make it easier for the tool to break up the joint line. The lower temperature on the retreating side of the tool may play a part in the formation of the joint line remnant.
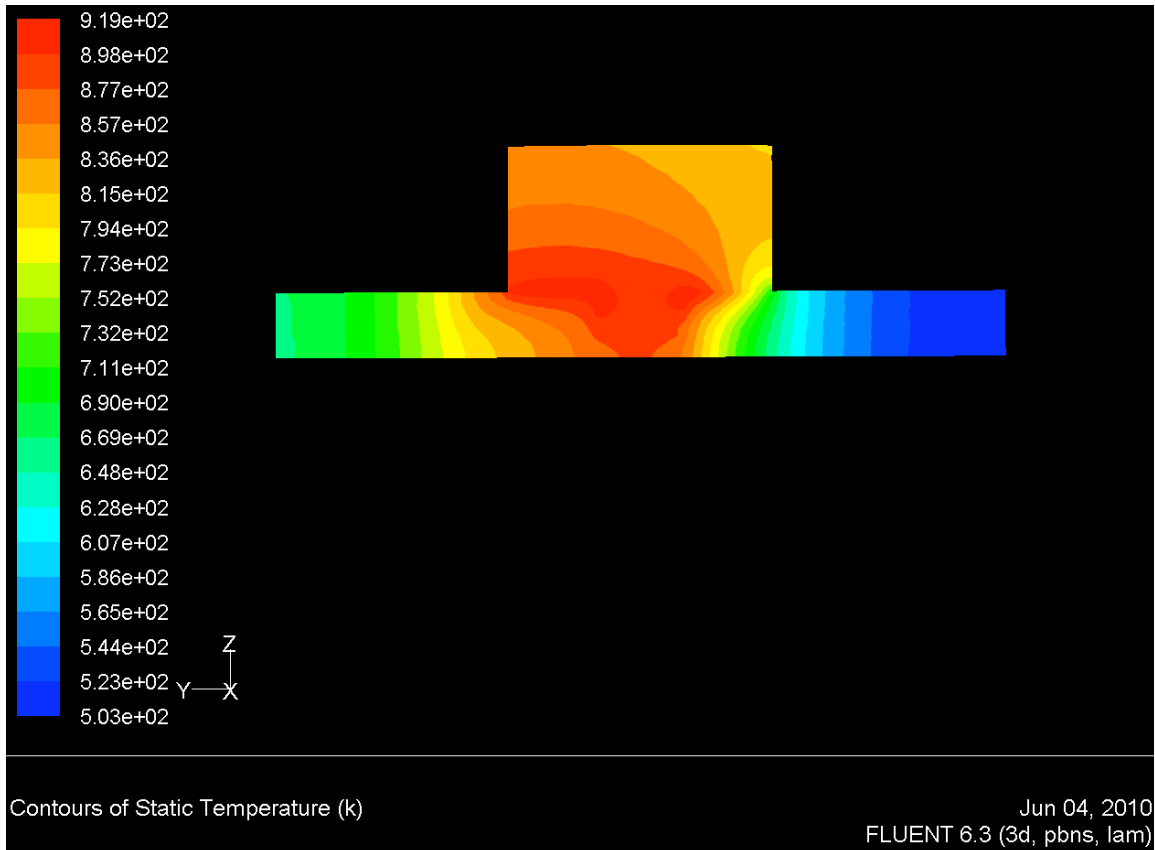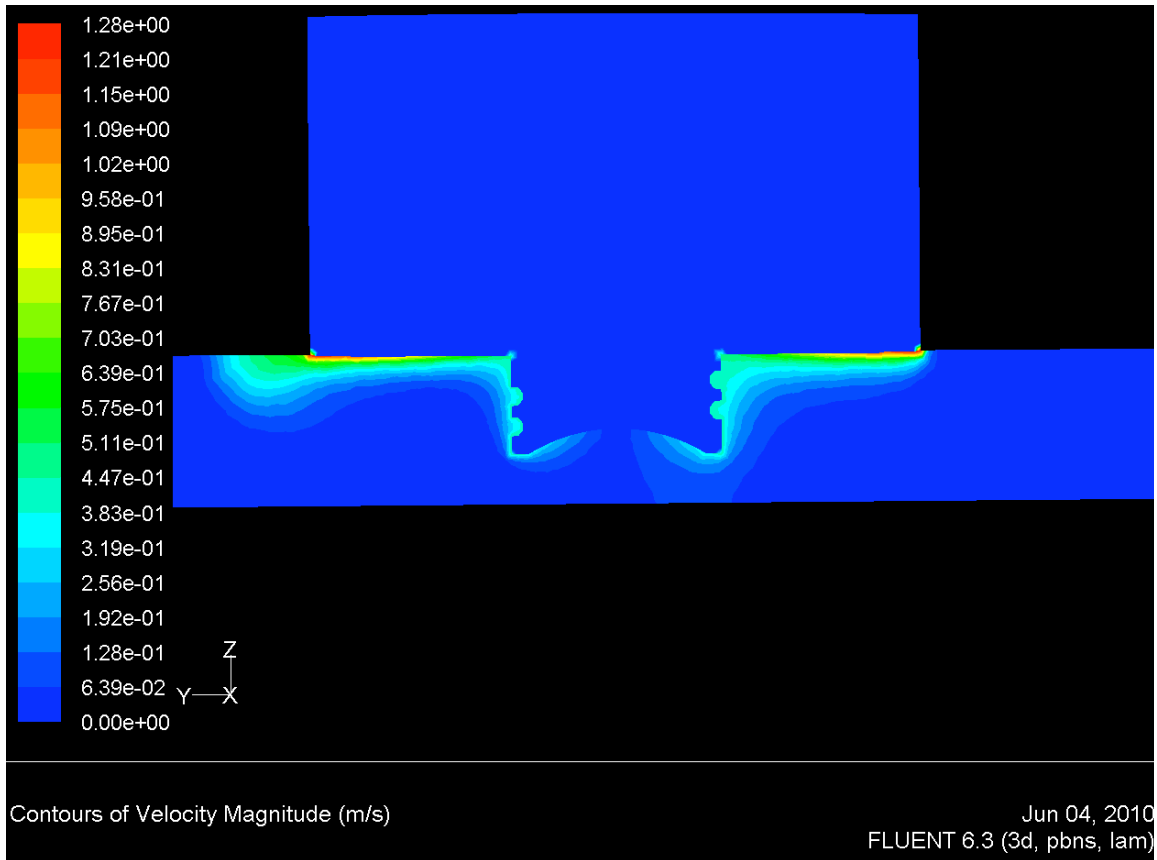
Figure 47 Velocity magnitudes found within the weld zone. The cross section view is taken halfway through the vertical tool plane. The advancing side is to the left of the tool.

The velocity profile of the pin (as seen in Figure 47) provides a closer look at the flow of material around the pin. There is some error on the advancing side that suggests material outside of the shoulder is being stirred which is experimentally known and observed to not be the case, and will not be considered. However, the model does show that the mechanical stirring does tend to favor the advancing side over the retreating, though not as pronounced as that observed in the temperature profiles. The tool exhibits excellent mixing in both the vertical and horizontal directions, although there is a section at the

center of the cup that appears to have no substantial material movement. This lack of movement appeared in one of the cross sectioned welds as a weld void (Figure 35 "d").
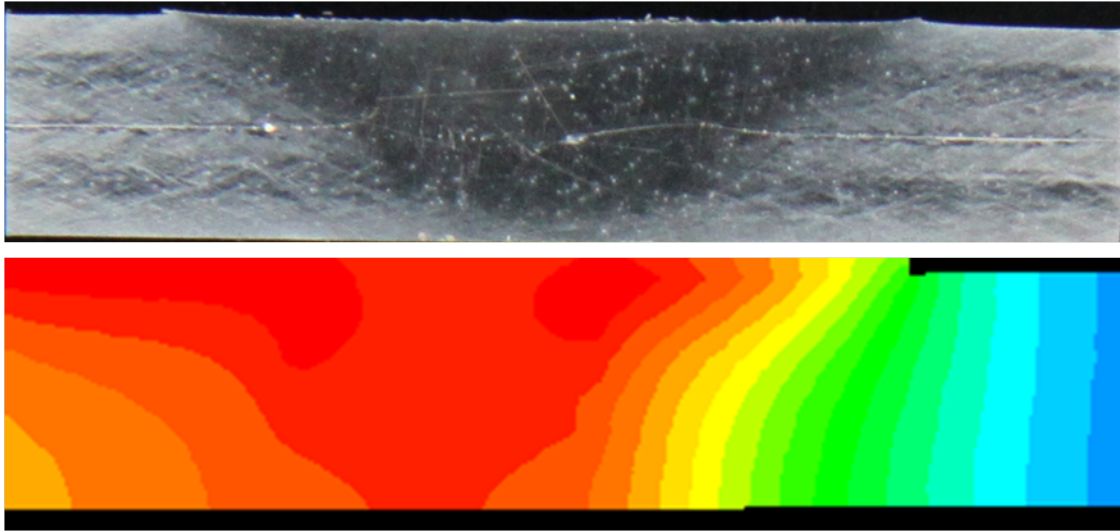
Figure 48 Comparison between CFD results and experimental cross sections

The experimental and CFD results are compared in Figure 48. The joint line remnant seen on the retreating side in the experimental cross sections is in good agreement with the significantly lower temperatures on the retreating side found in the CFD cross section. The red and very dark orange sections of Figure 48 represent the area of the weld zone that is between the solidus and liquidus temperatures. It can be seen that most of the weld zone on the retreating side of the weld is not within this temperature zone. Within this area on the macro-section it can be seen that there is no observable JLR. On the retreating side of the weld zone the temperature is below the solidus temperature and the presence of the JLR is very pronounced. The CFD model also manages to capture the general shape of the boundary of the TMAZ seen in the experimental cross sections and shows a good level of mixing top to bottom.

CHAPTER V

CONCLUSIONS

The results of the experiment showed a strong correlation between the resulting joint efficiency and the traverse/rotation speed of the tool. Unlike the majority of the findings in the literature, it was found that welding at higher traverse rates greatly increased the tensile strength of the welds. Similarly, increasing the rotation speed also increased the joint strength of the weld samples. The maximum ultimate tensile strength for both the 1500 and 2000 RPM welds occurred at 18 inches per minute and were 55.34% and 86.68% respectively. The lowest ultimate tensile strength for the 2000 RPM welds occurred at 2 inches per minute and was 33.3% of the parent sample.

The increased strength associated with the higher traverse rates is thought to be due to the reduced size of the grain structure as reported in the literature. Smaller grain sizes in the material increase the tensile strength and the ductility of the metal, which was observed in this experiment. The correlation between tensile strength and rotation speed is thought to be related to the increased strain (deformation) experienced by the workpiece. The higher rotation speeds increase the amount of deformation in the metal which helps to further refine the grain structure.

The higher rotation speeds inherently provide more stirring which helped break up the layer of oxide between the two plates. This layer of oxide can lead to a poor joint

line which may result in the formation of defects that can cause the welds to be weak. The increased stirring reduces the amount of the joint line remnant observed in the weld macro-sections but it does not eliminate it. Using a tool with a larger static pin to swept volume ratio (similar to the A-skew tool in Table 1) would promote more stirring and may help to eliminate the observed joint line remnants in each weld. The observation of the dispersoids within the weld zones can be attributed to the reactivity of the Mg AZ31B with the natural air environment during the weld. Repeating these welds in an inert environment such as a nitrogen or argon atmosphere may eliminate the formation of these dispersoids.

The results of the fluid dynamic model showed that there was a significant difference between the temperature gradient on the advancing side of the weld and that of the retreating side. It was found that a majority of the material on the advancing side was above the solidus temperature (605°C) while only a small portion of the weld on the retreating side was above this temperature. At this higher temperature, the material on the advancing side is softened, which increases the extent to which the material is plastically deformed (throughout the TMAZ). The absence of a joint line remnant (JLR) on the advancing side and the presence of the JLR on the retreating side may be an indication of an increase in stirring. Welding (FSW) Mg AZ31B above its solidus temperature results in a larger area of the HAZ that experiences plastic deformation. When Mg AZ31B is above the solidus point it begins to soften and increases the effectiveness of the FSW tool to stir (shear) the material.

It has been demonstrated that friction stir welding is a viable method for joining Mg AZ31B in a lap joint configuration with a single pass. High rotation speeds and

traverse speeds were found to produce the strongest welds. Experiments to help reduce the occurrence of the joint line remnant should be performed to further the understanding of joining this metal alloy. Different tool geometries and/or the welding procedure itself could be altered as previously mentioned to reduce the occurrence of defects.

1. Example of the rotation resulting from a tensile test on a lap weld sample. Hendricks et al. created a finite element model to capture the rotation of an Al6061 lap weld undergoing a tensile test. Note the out of plane rotation. The blue mesh represents the original part and the white mesh represents the deformed part.
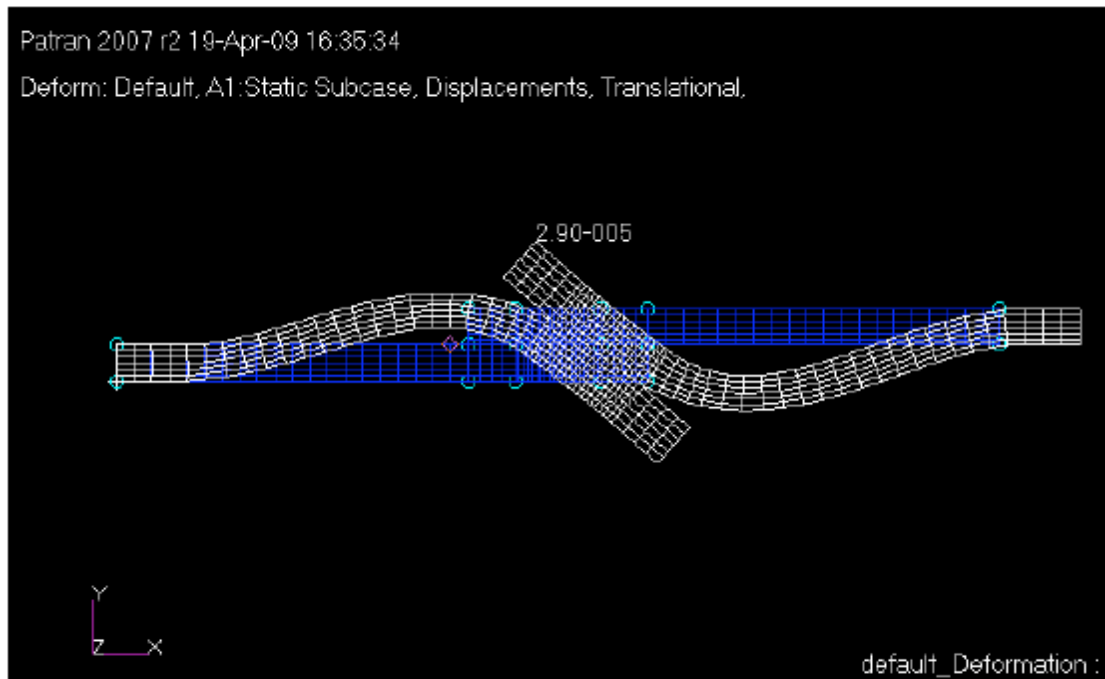
Appendix Figure 2 [Hendricks 2009]

2.The hooking defect occurs when the oxide layer between the top and bottom plate is not disrupted by the rotation of the pin. The appearance of the hooking defect can occur on both sides of the pin (advancing and retreating) and can reduce the strength of the weld. A drawing of the hooking defect can be seen below.

Ret.

Adv.

Appendix Figure 3. Drawing of the hooking defect observed in lap welds of Mg AZ31B. The black lines represent the hooking defect. This defect creates a stress concentration.

3. User Defined Function (UDF) used in FLUENT model to set an approximate viscosity

function of Mg AZ31B.

```c
#include "udf.h" /* must be at the beginning of every UDF you write */
#include "mem.h"
#include "metric.h"

DEFINE_PROPERTY(cell_viscosity, cell, thread) // define cell viscosity
{
real mu_lam;                              //
float x;
float Z;
float sinhinv; // in c-code log(number) Computes the ln of number
float stress_e;
real st = C_STRAIN_RATE_MAG(cell, thread); //strain rate in each cell, large matrix
real tem = C_T(cell, thread);
real alpha = 1/53.3 ; // 0.052 1/megapascals = 0.052 m^2/N Material Constant alpha
real n = 4.36;   // unit-less, Material Constant n
real Q = 129e3; // 130 KJ/mol = 130e3 J/mol Activation Energy
real A = 7.78e8; // 1/s Material Constant A
real R = 8.314472; // J/K-mol = J/K/mol = J/(K*mol)


if(st > 1 ){
Z = st*exp(Q/R/tem);
x = pow((Z/A),1/n);
sinhinv = log(x+sqrt(x*x+1));
stress_e = (1/alpha)*sinhinv;
mu_lam = (0.01*1e0+stress_e/(3*st))/(1e0+1);
}
else
{
mu_lam = (0.01*1e0+10)/(1e0+1);
;
}
return mu_lam;
}
```

**Appendix Figure 3 UDF created to approximate the viscosity of the plasticized
metal.**

REFERENCES

[Afrin 2008] Afrin, N., D. L. Chen, X. Cao, and M. Jahazi. "Microstructure and Tensile Properties of Friction Stir Welded AZ31B Magnesium Alloy." *Materials Science and Engineering A* 472 (2008): 179-86.

[Cao 2009] Cao, X., and M. Jahazi. "Effect of Welding Speed on Lap Joint Quality of Friction Stir Welded AZ31B." *Trends in Welding Research, Proceedings of the 8th International Conference* (2009): 72-80.

[Colegrove 2005] Colegrove, Paul A., and Hugh R. Shercliff. "3-Dimensional CFD Modelling of Flow Round a Threaded Friction Stir Welding Tool Profile." *Journal of Materials Processing Technology* 169 (2005): 320-27.

[Cox 2010] Cox, Chase D., David H. Lammlein, Alvin M. Strauss, and George E. Cook. "Modeling the Control of an Elevated Tool Temperature and the Affects on Axial Force During Friction Stir Welding." *Journal of Materials and Manufacturing Processes*, Accepted for publication (2010).

[Crawford 2006] Crawford, R., Cook, G. E., Strauss, A. M., Hartman, D. A., Stremler, M. A. "Experimental defect analysis and force prediction simulation of high weld pitch friction stir welding." *Science and Technology of Welding & Joining*, 11(6):657-665, 2006

[De Vuyst 2007] De Vuyst, T., Magotte, O., Robineau, A., Goussian J-C, Alvise LD; Multi-physics simulation of the material flow and temperature field around FSW tool: *Proc. of the 6th International Symposium on Friction Stir Welding*, 2007.

[Elektron 2006] *Elektron AZ31B Sheet, Plate and Coil*. Data Sheet: 482. Magnesium Elektron UK, May 2006. Web. <www.magnesium-elektron.com>.

[Esparza 2002] Esparza, J. A., W. C. Davis, E. A. Trillo, and L. E. Murr. "Friction-stir welding of magnesium alloy AZ31B." *J. of Materials Science Letters* 21 (2002): 917-20.

[Hendricks 2009] Hendricks, Chris E. *The Mechanical Effects of Weavetrack on Friction Stir Welds in a Lap Joint Configuration*. M.S. Thesis. Vanderbilt University, 2009.

[Int. Mg 2007] International Magnesium Association. "Magnesium Fosters Rebirth of an Automotive Engine." *Mg Showcase*. 1 May 2007. Web. 29 June 2010. <http://www.intlmag.org/files/mg001.pdf>.

[Jones 2007] Jones, Tyrone L., Matthew S. Burkins, and William A. Gooch. *An Analysis of Magnesium Alloy AZ31B-H24 for Ballistic Applications*. Tech. Report no. ARL-TR-4327. Army Research Laboratory, 2007.

[Kumar 2010] Kumar, K., and S. V. Kailas. "Positional Dependence of Material Flow in Friction Stir Welding: Analysis of Joint Line Remnant and Its Relevance to Dissimilar Metal Welding." *Science and Technology of Welding and Joining* 15.4 (2010): 305-311.

[Lammlein 2009] Lammlein, D.H., DeLapp, D.R., Fleming, P.A., Strauss, A.M., Cook, G.E. The application of shoulderless conical tools in friction stir welding: An experimental and theoretical study. *Materials & Design*, 30 (2009): 4012-4022.

[Lammlein 2009b] Lammlein, D.H., Longhurst, W.R., DeLapp, D.R., Fleming, P.A., Strauss, A.M., Cook, G.E. The Friction Stir Welding of Hemispheres : A technique for Manufacturing Hollow Spheres *The Int. Journal of Advanced Manufacturing Technology*, Submitted for publication 2009.

[Lee 2002] Lee, Won-Bae, Shae K. Kim, Young-Jig Kim, and Seong-Boo Jung. "Microstructure and Mechanical Properties of Friction Stir Welded AZ31 Mg Alloy." Magnesium Technology (2002).

[Lee 2003] Lee, W. B., Y. M. Yeon, and S. B. Jung. "Joint properties of friction stir welded AZ31B-H24 magnesium alloy." *Materials Science and Technology* 19 (2003): 785-90.

[Logan 2007] Logan, Daryl L. *A First Course in the Finite Element Method*. Toronto, Canada: Thomson, 2007.

[Magnesium 2010] "Magnesium." *Wikipedia, the Free Encyclopedia*. Web. 08 June 2010. http://en.wikipedia.org/wiki/Magnesium

[McGonigal 1962] McGonigal, P. J., A. D. Kirshenbaum, and A. V. Grosse. "The Liquid Temperature Range, Density, and Critical Constants of Magnesium." *J. Phys. Chem*. 66 (1962): 737-39.

[Mishra 2005] Mishra, R. S., and Z. Y. Ma. "Friction Stir Welding and Processing." *Materials Science and Engineering* R 50 (2005): 1–78.

[Mordike 2001] Mordike, B. L., and T. Ebert. "Magnesium: Properties, applications, potential." *Materials Science and Engineering* A302 (2001): 37-45.

[Nandan 2008] Nandan, R., T. DebRoy, and H.K.D.H. Bhadeshia. "Recent advances in friction stir welding Process, weldment structure and properties." *Progress in Materials Science* 53 (2008): 980-1023.

[Pareek 2007] Pareek, M., A. Polar, F. Rumiche, and J. E. Indacochea. "Metallurgical Evaluation of AZ31B-H24 Magnesium Alloy Friction Stir Welds." *Journal of Materials Engineering and Performance* 16.5 (2007): 655-62.

[Santiago 2004] Santiago DH, Lombera G, Santiago U; Numerical modeling of welded joints by the friction stir welding process; *Materials Research* 7.4, (2004): 569-574.

[Sellars 1966] Sellars, C., Tegart, W. M.: "On the mechanism of hot deformation", *Acta Met.*, 14.9 (1966): 1136-1138

[Sinclair 2009] P. Sinclair, W.R. Longhurst, C. Cox, D.H. Lammlein, A.M. Strauss, G.E. Cook. Heated Friction Stir Welding: An Experimental and Theoretical Investigation into how Preheating Influences on Process Forces *Materials and Manufacturing Processes*, Accepted for publication 2010.

[Spigarelli 2001] Spigarelli, S., E. Evangelista, E. Cerri, and T. G. Langdon. "Constitutive Equations for Hot Deformation of an Al-6061/20%Al2O3 Composite." *Materials Science and Engineering A* 319-321 (2001): 721-25.

[Tello 2010] Tello, K. E., A. P. Gerlich, and P. F. Mendez. "Constants for Hot Deformation Constitutive Models for Recent Experimental Data." *Science and Technology of Welding and Joining* 15.3 (2010): 260-66.

[Threadgill 2007] Threadgill P. "Terminology in friction stir welding". *Science and Technology of Welding and Joining*. 12 (2007): 357-360.

[TWI 2010] Thomas, Wayne, David Staines, and Ian Norris. "Novel Developments in Friction Stir Welding. (Connect May 2002)." *TWI - Welding and Joining Specialist*. The Welding Institute. Web. 23 June 2010. <http://www.twi.co.uk/content/c1183.html>.

[DOE 1993] United States. Department of Energy. *DOE Fundamentals Handbook Material Science Volume 1 of 2*. National Technical Information Service, Jan. 1993. Web.